

# Passive Imaging with Ambient Noise Under Wave Speed Mismatch: Mathematical Analysis and Wave Speed Estimation

Zetao Fei\* and Josselin Garnier†

February 18, 2026

## Abstract

It is known that waves generated by ambient noise sources and recorded by passive receivers can be used to image the reflectivities of an unknown medium. However, reconstructing the reflectivity of the medium from partial boundary measurements remains a challenging problem, particularly when the background wave speed is unknown. In this paper, we investigate passive correlation-based imaging in the daylight configuration, where uncontrolled noise sources illuminate the medium and only ambient fields are recorded by a sensor array. We first analyze daylight migration for a point reflector embedded in a homogeneous background. By introducing a searching wave speed into the migration functional, we derive an explicit characterization of the deterministic shift and defocusing effects induced by wave-speed mismatch. We show that the maximum of the envelope of the resulting functional provides a reliable estimator of the true wave speed. We then extend the analysis to a random medium with correlation length smaller than the wavelength. Leveraging the shift formula obtained in the homogeneous case, we introduce a virtual guide star that remains fixed under migration with different searching speeds. This property enables an effective wave-speed estimation strategy based on spatial averaging around the virtual guide star. For both homogeneous and random media, we establish resolution analyses for the proposed wave-speed estimators. Numerical experiments are conducted to validate the theoretical result.

## 1 Introduction

Passive correlation-based imaging reconstructs information about a medium or subsurface using only wave-fields transmitted by opportunistic or ambient noise sources. This technique was first demonstrated experimentally in [1] and has since gained widespread use in various fields, including helioseismology [2], volcano monitoring [3], and reservoir monitoring [4]. For a broad interdisciplinary review of correlation-based methods, we refer the reader to [5]; an extensive overview of the mathematical foundations can be found in the monograph [6].

It is now well understood that key information—such as travel times and Green functions—is encoded in the cross-correlation of recorded signals [7]–[10]. This observation underlies the success of imaging reflectors using migration of the empirical cross-correlation. In [11], the authors developed a unified mathematical framework for analyzing passive imaging across diverse configurations. The uniqueness of passive imaging inverse problems has also been established in both the time and frequency domains; see, for instance, [12], [13].

In this paper, we focus on passive imaging in the *daylight configuration*, where a sensor array is located between randomly distributed noise sources and the medium of interest. This setting is common in the literature on virtual-source imaging, where the receiver acts as a virtual source. The scattered waves recorded at the array are numerically back-propagated as if emitted from the receiver, allowing wavefield reconstruction and improved focusing in complex media. This method is widely used in seismic exploration [14]–[16], and

\*CMAP, Ecole Polytechnique, Institut Polytechnique de Paris, 91120 Palaiseau, France (zetao.fei@polytechnique.edu).

†CMAP, CNRS, Ecole Polytechnique, Institut Polytechnique de Paris, 91120 Palaiseau, France (josselin.garnier@polytechnique.edu). This work was partially supported by Agence Nationale de la Recherche (Grant No. ANR-23-CE30-0021).

its mathematical foundations are discussed in [17]. We first investigate the case of a point-like reflector embedded in a homogeneous background, a geometry closely related to classical reflector-imaging problems. Cross-correlation based method in this setting has been validated in physical experiments [18] and widely applied in seismology, e.g., [19]–[21]. A detailed resolution analysis of this approach was provided in [22], [23]. We then extend the proposed method to the a second scenario in which the medium is random, with a correlation length much smaller than the wavelength. We emphasize that the setup considered in this paper differs from typical virtual-source imaging: in our case, there is no controlled source array, and the imaging functional in daylight geometry takes a different form. Nevertheless, the underlying idea remains similar—recovering information about the medium of interest from the scattered field generated under uncontrolled (daylight) illumination.

A major focus of this work concerns the estimation of the background wave speed from partial passive boundary measurements. Accurate knowledge of the background wave speed is crucial in passive imaging, both for properly focusing the image and for interpreting medium properties. Eikonal-based methods are widely used for wave-speed estimation in ambient noise tomography [24], [25]; see also the review [26]. However, their implementation in a daylight configuration is challenging. Optimization-based approaches such as Full Waveform Inversion (FWI) [27], [28] offer an alternative strategy by minimizing the discrepancy between recorded and simulated data, and recent efforts have extended such methods to quantitative passive imaging [29]. Nonetheless, these techniques remain computationally demanding and suffer from intrinsic non-convexity. In the literature, cross-correlation-based methods have been applied to image media with three-dimensional rapid fluctuations and a one-dimensional slowly varying background in the parabolic regime [30]. However, to our knowledge, few studies have considered estimating the effective wave speed in a random medium under passive, daylight-type illumination.

In the context of active imaging, recent developments in aberration correction and wave-speed estimation using reflection-matrix analysis have introduced techniques that do not require a strong guide star (i.e. a point-like strong reflector). These methods exploit the recorded backscattered field by generating a synthetic focus that acts as a virtual guide star [31]–[33]. This idea motivates the introduction of a virtual guide star in our passive imaging setting. A mathematical framework for interpreting such experiments was recently proposed in [34], and a related concept has been explored in passive imaging in [35].

The contributions of this paper are summarized below. First, in the daylight configuration with a point-like reflector in a homogeneous background, we introduce a searching wave speed  $c_s$  into the traditional daylight imaging functional and derive a quantitative characterization of the effects of wave-speed mismatch. Our analysis shows how an incorrect wave speed leads to shifts and blurring in the reconstructed reflector location. We further demonstrate that the maximum of the envelope of the generalized imaging functional yields a robust estimator for the background wave speed. Second, we extend this methodology to the random-medium setting, where no strong guide star is present. By migrating the empirical cross-correlation using different searching wave speeds, we construct a virtual guide star whose physical location is stabilized by the analytical shifting formula established in the homogeneous case (see (3.8)). The background wave speed is then estimated from spatial averages of the imaging functional around this virtual guide star. For both settings, we provide a comprehensive theoretical analysis, including resolution properties, and validate the proposed estimators through numerical experiments.

The remainder of the paper is organized as follows. Section 2 introduces the mathematical framework and reviews key properties of cross-correlation in passive imaging. Section 3 analyzes the generalized daylight migration imaging functional in the presence of a point-like reflector and presents a wave-speed estimator. Section 4 extends the method to random media and introduces the virtual guide-star-based estimator. Numerical experiments are given in Section 5, and concluding remarks appear in Section 6.

## 2 Preliminaries

In this section, we present the mathematical models and assumptions underlying the problem studied in this paper. Section 2.1 provides a detailed description of the problem setup. In Section 2.2, we briefly review key properties of cross-correlation, a fundamental tool in passive imaging. For a more comprehensive discussion, we refer the reader to [6].

## 2.1 Problem Outline

We consider the scalar wavefield  $u$  governed by the inhomogeneous acoustic wave equation

$$\frac{1}{c^2(\mathbf{x})} \frac{\partial^2 u}{\partial t^2} - \Delta_{\mathbf{x}} u = n(t, \mathbf{x}), \quad (2.1)$$

where  $c(\mathbf{x})$  denotes the spatially varying wave speed and  $n(t, \mathbf{x})$  is a random noise field. The noise is assumed to be zero-mean and stationary in time, with frequency band  $\mathcal{B}$  centered at  $\omega_c$  and bandwidth  $B$ . Its second-order statistics are specified by

$$\mathbb{E}[n(t_1, \mathbf{y}_1)n(t_2, \mathbf{y}_2)] = F_\varepsilon(t_2 - t_1) \Gamma(\mathbf{y}_1, \mathbf{y}_2), \quad (2.2)$$

where  $F_\varepsilon$  encodes the temporal correlation and satisfies  $F_\varepsilon(0) = 1$ . Its Fourier transform,

$$\widehat{F}_\varepsilon(\omega) = \int_{\mathbb{R}} F_\varepsilon(t) e^{i\omega t} dt,$$

is real-valued, even, nonnegative, and proportional to the source power spectral density. We assume that the decoherence time of the sources is short relative to the typical travel times. Introducing a small scale parameter  $\varepsilon \ll 1$ , we write

$$F_\varepsilon(t) = F\left(\frac{t}{\varepsilon}\right), \quad (2.3)$$

so that the central frequency scales as  $\omega_c = \omega_0/\varepsilon$ , and the bandwidth scales as  $B = B_H/\varepsilon$ .

Spatially, the sources are taken to be delta-correlated:

$$\Gamma(\mathbf{y}_1, \mathbf{y}_2) = K(\mathbf{y}_1) \delta(\mathbf{y}_1 - \mathbf{y}_2),$$

where  $K$  describes their spatial distribution.

**Medium model.** The wave speed is described as a small perturbation of a homogeneous background:

$$\frac{1}{c^2(\mathbf{x})} = \frac{1}{c_0^2} (1 + \rho(\mathbf{x})).$$

We consider two types of perturbations:

- **Point-like reflector.** A compact reflector located near  $\mathbf{z}_r$  is modeled by

$$\rho(\mathbf{x}) = \sigma_r V_r(\mathbf{x}), \quad V_r(\mathbf{x}) = \mathbb{1}_{\Omega_r}(\mathbf{x} - \mathbf{z}_r),$$

where  $\Omega_r$  has characteristic size  $\ell_r$ . The point-reflector regime corresponds to  $\ell_r \ll \lambda$ , and the reflector is assumed weak,  $\sigma_r \ll 1$ . Neither the reflector position  $\mathbf{z}_r$  nor the background velocity  $c_0$  is assumed to be known.

- **Random medium.** In this regime, the perturbations are supported in a region  $\mathcal{D}$  and modeled by a rapidly oscillatory random field:

$$\rho(\mathbf{x}) = \rho_\mu(\mathbf{x}) = \mu\left(\frac{\mathbf{x}}{\ell_c}\right), \quad \mathbf{x} \in \mathcal{D},$$

where  $\ell_c \ll \lambda$  is the correlation length. The random field  $\mu$  is assumed to be stationary, mean-zero, and has covariance function

$$\Sigma(\mathbf{x}) = \text{Cov}(\mu(\mathbf{x}), \mu(0)),$$

decaying at the rate  $|\Sigma(\mathbf{x})| \lesssim (1 + |\mathbf{x}|)^{-4-\eta}$  for some  $\eta > 0$ . The fluctuations are assumed weak,  $|\Sigma(0)| \ll 1$ . While the mean-zero assumption is restrictive theoretically, it is not an obstacle in practice because the boundary reflections due to a nonzero mean can be mitigated or are negligible in the imaging geometry presented below.

**Data acquisition geometry.** We work in a passive *daylight* configuration in which an array  $\mathcal{A}$  records the signals  $u(t, \mathbf{x}_j)$ ,  $j = 1, \dots, N$ , and is positioned between the random noise sources (i.e. the support of  $K$ ) and the medium of interest (i.e.  $\mathbf{z}_r$  or  $\mathcal{D}$ ). The short decoherence time implies a high central frequency. The array radius  $a$  is assumed larger than the wavelength  $\lambda$ , but smaller than the distance to the reflector  $|\mathbf{z}_r|$ . Under the scaling (2.3), we write

$$\omega_c = \frac{\omega_0}{\varepsilon}, \quad \lambda = \varepsilon \frac{2\pi c_0}{\omega_0}, \quad a = \varepsilon^{1/2} a_0,$$

and parameterize the array as  $\mathcal{A} = a \mathcal{A}_0$  for some reference geometry  $\mathcal{A}_0$ . Here, we assume that the typical travel distance is much larger than the wavelength with  $\text{dist}(\mathbf{z}_r, \mathcal{A}) \sim 1$  or  $\text{dist}(\mathcal{D}, \mathcal{A}) \sim 1$ .

The primary goal of this paper is to propose estimators for the background wave speed  $c_0$  for both configurations and to localize the point-like reflector in the first configuration. Figure 1 illustrates the daylight configuration for the point-reflector and random-medium setups.

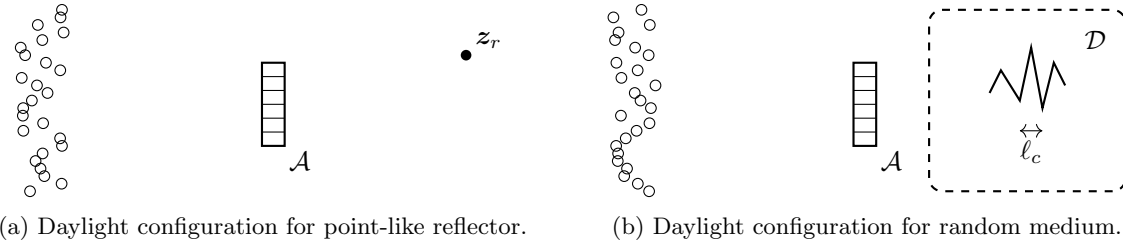


Figure 1: Daylight configuration for passive imaging of two different types of medium.

## 2.2 Cross-correlation and imaging functional

We start the introduction to the cross-correlation with the representation of the wave function (2.1). By the formulation provided previously, the solution to the wave equation has the following integral representation:

$$u(t, \mathbf{x}) = \iint ds dy \, n(t-s, \mathbf{y}) G(s, \mathbf{x}, \mathbf{y}). \quad (2.4)$$

The function  $G$  is the time-dependent causal Green's function, i.e., the fundamental solution to the equation

$$\begin{cases} \frac{1}{c^2(\mathbf{x})} \frac{\partial^2 G}{\partial t^2} - \Delta_{\mathbf{x}} G = \delta(t) \delta(\mathbf{x} - \mathbf{y}) \\ G(t, \mathbf{x}, \mathbf{y}) = 0, \quad \forall t < 0. \end{cases} \quad (2.5)$$

We also introduce the time-harmonic Green's function  $\widehat{G}_0$  for the background homogeneous medium, i.e., the solution to the Helmholtz equation

$$\begin{cases} \Delta_{\mathbf{x}} \widehat{G}_0 + \frac{\omega^2}{c_0^2} \widehat{G}_0 = -\delta(\mathbf{x} - \mathbf{y}), \\ \lim_{|\mathbf{x}| \rightarrow \infty} |\mathbf{x}| \left( \frac{\mathbf{x}}{|\mathbf{x}|} \cdot \nabla_{\mathbf{x}} - i \frac{\omega}{c_0} \right) \widehat{G}_0(\omega, \mathbf{x}, \mathbf{y}) = 0. \end{cases} \quad (2.6)$$

We consider the empirical cross-correlation over a time interval  $(0, T)$  of the signal recorded at  $\mathbf{x}_1, \mathbf{x}_2 \in \mathcal{A}$  defined by

$$C_T(\tau, \mathbf{x}_1, \mathbf{x}_2) = \frac{1}{T} \int_0^T u(t, \mathbf{x}_1) u(t + \tau, \mathbf{x}_2) dt. \quad (2.7)$$

The statistical stability of the above quantity is well established, as shown in the following proposition [6]:

**Proposition 2.1.** (1) *The expectation of the empirical cross-correlation  $C_T$  (with respect to the statistical law of the sources) is independent of  $T$ :*

$$\mathbb{E} C_T(\tau, \mathbf{x}_1, \mathbf{x}_2) = C^{(1)}(\tau, \mathbf{x}_1, \mathbf{x}_2). \quad (2.8)$$

The theoretical (or statistical) cross-correlation  $C^{(1)}$  is given by

$$C^{(1)}(\tau, \mathbf{x}_1, \mathbf{x}_2) = \frac{1}{2\pi} \iint d\mathbf{y} d\omega \widehat{F}(\omega) K(\mathbf{y}) \overline{\widehat{G}(\omega, \mathbf{x}_1, \mathbf{y})} \widehat{G}(\omega, \mathbf{x}_2, \mathbf{y}) e^{-i\omega\tau}, \quad (2.9)$$

where  $\widehat{G}(\omega, \mathbf{x}, \mathbf{y})$  is the time-harmonic Green's function, that is, the Fourier transform of  $G(t, \mathbf{x}, \mathbf{y})$ , and the overline stands for complex conjugation.

(2) The empirical cross-correlation  $C_T$  is a self-averaging quantity:

$$C_T(\tau, \mathbf{x}_1, \mathbf{x}_2) \xrightarrow{T \rightarrow \infty} C^{(1)}(\tau, \mathbf{x}_1, \mathbf{x}_2), \quad (2.10)$$

in probability with respect to the statistical law of the sources.

With the recorded signals  $\{u(t, \mathbf{x}_j)\}_{t \in \mathbb{R}, j=1, \dots, N}$ , we compute the corresponding cross-correlations. The inverse problem considered in this paper is then reformulated as extracting information about the medium from the data set  $\{C_T\}$ . To this end, we introduce the *generalized daylight migration imaging functional*

$$\mathcal{I}(\mathbf{z}_s, c_s) = \sum_{j, l=1}^N C_T(\mathcal{T}_s(\mathbf{z}_s, \mathbf{x}_l) + \mathcal{T}_s(\mathbf{z}_s, \mathbf{x}_j), \mathbf{x}_j, \mathbf{x}_l), \quad (2.11)$$

where  $\mathbf{z}_s$  denotes the search point,  $c_s$  is the sound speed used in migration, and  $\mathcal{T}_s(\mathbf{z}_s, \mathbf{x})$  is the generalized travel time defined by

$$\mathcal{T}_s(\mathbf{z}_s, \mathbf{x}) := \frac{|\mathbf{z}_s - \mathbf{x}|}{c_s}.$$

Furthermore, we denote the ratio of  $c_s$  and  $c_0$  by  $v = c_s/c_0$ . When  $c_s = c_0$  (i.e.  $v = 1$ ),  $\mathcal{T}_s$  coincides with the travel time in a homogeneous medium,

$$\mathcal{T}_0(\mathbf{z}_s, \mathbf{x}) := \frac{|\mathbf{z}_s - \mathbf{x}|}{c_0},$$

and the imaging functional reduces to the classical daylight migration functional.

In the dense-array limit, the imaging functional can be approximated by

$$\mathcal{I}(\mathbf{z}_s, c_s) = \frac{N^2}{|\mathcal{A}|^2} \iint_{\mathcal{A}^2} d\mathbf{x}_1 d\mathbf{x}_2 C_T(\mathcal{T}_s(\mathbf{z}_s, \mathbf{x}_2) + \mathcal{T}_s(\mathbf{z}_s, \mathbf{x}_1), \mathbf{x}_1, \mathbf{x}_2). \quad (2.12)$$

The construction of the imaging functional motivates the analysis of the theoretical cross-correlation  $C^{(1)}$ . Under the assumption that the perturbation of the background medium is weak, we may invoke the Born approximation for the Green's function,

$$\widehat{G}(\omega, \mathbf{x}, \mathbf{y}) \simeq \widehat{G}_0(\omega, \mathbf{x}, \mathbf{y}) + \frac{\omega^2}{c_0^2} \int dz \tilde{\rho}(z) \widehat{G}_0(\omega, \mathbf{x}, z) \widehat{G}_0(\omega, z, \mathbf{y}), \quad (2.13)$$

where

$$\tilde{\rho}(z) = \begin{cases} \sigma_r \ell_r^3 \delta(z - z_r), & \text{point-like reflector,} \\ \rho_\mu(z), & \text{random medium.} \end{cases}$$

Combining (2.9), (2.13), and the scaling regime introduced in the previous section, we obtain the decomposition

$$C^{(1)}(\tau, \mathbf{x}_1, \mathbf{x}_2) = C_0^{(1)}(\tau, \mathbf{x}_1, \mathbf{x}_2) + C_i^{(1)}(\tau, \mathbf{x}_1, \mathbf{x}_2) + C_{ii}^{(1)}(\tau, \mathbf{x}_1, \mathbf{x}_2), \quad (2.14)$$

where

$$C_0^{(1)}(\tau, \mathbf{x}_1, \mathbf{x}_2) = \frac{1}{2\pi} \iint d\mathbf{y} d\omega K(\mathbf{y}) \widehat{F}(\omega) \overline{\widehat{G}_0(\frac{\omega}{\varepsilon}, \mathbf{x}_1, \mathbf{y})} \widehat{G}_0(\frac{\omega}{\varepsilon}, \mathbf{x}_2, \mathbf{y}) e^{-i\frac{\omega\tau}{\varepsilon}},$$

$$C_i^{(1)}(\tau, \mathbf{x}_1, \mathbf{x}_2) = \frac{1}{2\pi c_0^2 \varepsilon^2} \int dz \tilde{\rho}(z) \iint d\mathbf{y} d\omega \omega^2 K(\mathbf{y}) \widehat{F}(\omega) \widehat{G}_0(\frac{\omega}{\varepsilon}, \mathbf{x}_2, z) \widehat{G}_0(\frac{\omega}{\varepsilon}, z, \mathbf{y}) \overline{\widehat{G}_0(\frac{\omega}{\varepsilon}, \mathbf{x}_1, \mathbf{y})} e^{-i\frac{\omega\tau}{\varepsilon}},$$

$$C_{ii}^{(1)}(\tau, \mathbf{x}_1, \mathbf{x}_2) = \frac{1}{2\pi c_0^2 \varepsilon^2} \int dz \tilde{\rho}(z) \iint d\mathbf{y} d\omega \omega^2 K(\mathbf{y}) \widehat{F}(\omega) \overline{\widehat{G}_0(\frac{\omega}{\varepsilon}, \mathbf{x}_1, z)} \overline{\widehat{G}_0(\frac{\omega}{\varepsilon}, z, \mathbf{y})} \widehat{G}_0(\frac{\omega}{\varepsilon}, \mathbf{x}_2, \mathbf{y}) e^{-i\frac{\omega\tau}{\varepsilon}}.$$

The term  $C_0^{(1)}$  corresponds to the contribution of the direct waves, and it involves the rapid phase

$$\frac{\omega}{\varepsilon} \left( \frac{|\mathbf{x}_2 - \mathbf{y}|}{c_0} - \frac{|\mathbf{x}_1 - \mathbf{y}|}{c_0} - \tau \right).$$

For fixed  $\mathbf{x}_1, \mathbf{x}_2 \in \mathcal{A}$ , this contribution is supported on the time interval  $[-\Delta\tau_0, \Delta\tau_0]$ , where

$$\Delta\tau_0 := \frac{\sup_{\mathbf{y} \in \text{supp}(K)} |\mathbf{y} - \mathbf{x}_1| - |\mathbf{y} - \mathbf{x}_2|}{c_0} \leq \frac{|\mathbf{x}_1 - \mathbf{x}_2|}{c_0} \leq \frac{\text{diam}(\mathcal{A})}{c_0},$$

which is of order  $\mathcal{O}(\varepsilon^{\frac{1}{2}})$  in the regime under consideration.

In contrast, the scattered-wave contributions  $C_I^{(1)}$  and  $C_{II}^{(1)}$  involve the rapid phases

$$\frac{\omega}{\varepsilon} \left( \frac{|\mathbf{x}_2 - \mathbf{z}|}{c_0} + \frac{|\mathbf{z} - \mathbf{y}|}{c_0} - \frac{|\mathbf{x}_1 - \mathbf{y}|}{c_0} - \tau \right) \quad \text{and} \quad \frac{\omega}{\varepsilon} \left( \frac{|\mathbf{x}_2 - \mathbf{y}|}{c_0} - \frac{|\mathbf{z} - \mathbf{y}|}{c_0} - \frac{|\mathbf{x}_1 - \mathbf{z}|}{c_0} - \tau \right),$$

respectively. Recall that we consider the daylight configuration in this paper, these terms are supported on time intervals satisfying

$$|\tau| \asymp \frac{2 \text{ dist}(\mathbf{z}_r, \mathcal{A})}{c_0} \quad \text{or} \quad |\tau| \asymp \frac{2 \text{ dist}(\mathcal{D}, \mathcal{A})}{c_0},$$

both of which are quantities of order one. Consequently, within the considered regime, the direct and scattered contributions to the cross-correlation are well separated in time. Therefore, the component  $C_0^{(1)}$  can be effectively removed from the recorded data by time-windowing.

In the remainder of the analysis, we focus exclusively on the scattered-wave contributions. With a slight abuse of notation, we therefore redefine

$$C^{(1)}(\tau, \mathbf{x}_1, \mathbf{x}_2) = C_I^{(1)}(\tau, \mathbf{x}_1, \mathbf{x}_2) + C_{II}^{(1)}(\tau, \mathbf{x}_1, \mathbf{x}_2). \quad (2.15)$$

### 3 Guide star assisted wave speed estimation

In this section, we analyze the properties of the imaging functional  $\mathcal{I}(\mathbf{z}_s, c_s)$  defined in (2.11) when a point-like reflector is present in the medium. The analysis quantitatively characterizes the influence of wave speed mismatch on the point spread function, including the phenomenon of focusing point shift. Based on these insights, we propose methods for estimating the background wave speed  $c_0$  and localizing the point-like reflector.

#### 3.1 Analysis of the imaging functional

To present the properties of the imaging functional, we first introduce a coordinate frame  $(\hat{\mathbf{e}}_1, \hat{\mathbf{e}}_2, \hat{\mathbf{e}}_3)$  satisfying

- the sensor array is centered around  $\mathbf{0}$  and  $\mathcal{A} \subset \text{span}\{\hat{\mathbf{e}}_1, \hat{\mathbf{e}}_2\}$ ,
- the reflector  $\mathbf{z}_r \in \text{span}\{\hat{\mathbf{e}}_1, \hat{\mathbf{e}}_3\}$  with coordinates  $\mathbf{z}_r = (\mathbf{z}_{r,1}, 0, \mathbf{z}_{r,3})$ .

Recall the regime we adopt for the sensor array, for  $\mathbf{x}_1 \in \mathcal{A}$ , we write  $\mathbf{x}_1 = \varepsilon^{\frac{1}{2}} \widetilde{\mathbf{x}_1} = \varepsilon^{\frac{1}{2}} (\widetilde{\mathbf{x}_{1,1}}, \widetilde{\mathbf{x}_{1,2}}, 0)$ .

We also introduce the following orthonormal frame  $\{\hat{\mathbf{f}}_1, \hat{\mathbf{f}}_2, \hat{\mathbf{f}}_3\}$ :

$$\hat{\mathbf{f}}_1 = \frac{1}{|\mathbf{z}_r|} (\mathbf{z}_{r,3} \hat{\mathbf{e}}_1 - \mathbf{z}_{r,1} \hat{\mathbf{e}}_3), \quad \hat{\mathbf{f}}_2 = \hat{\mathbf{e}}_2, \quad \hat{\mathbf{f}}_3 = \frac{1}{|\mathbf{z}_r|} (\mathbf{z}_{r,1} \hat{\mathbf{e}}_1 + \mathbf{z}_{r,3} \hat{\mathbf{e}}_3). \quad (3.1)$$

Different from the traditional daylight migration imaging functional, in  $\mathcal{I}(\mathbf{z}_s, c_s)$ , the speed of sound used for backpropagation  $c_s$  can have a mismatch with  $c_0$ . This mismatch can lead to a shift in the focusing point of the image derived from  $\mathcal{I}(\mathbf{z}_s, c_s)$ . A similar phenomenon is observed in the active imaging configuration,

see [34]. We denote the focusing point in the image as  $\mathbf{z}_f(v)$ , and  $\mathbf{z}_f$  when there is no ambiguity. We define the map  $\phi_v : \mathbb{R}^3 \rightarrow \mathbb{R}^3$  as

$$\phi_v(\mathbf{z}_r) = \left( v^2 \mathbf{z}_r^\perp, v \sqrt{(\mathbf{z}_r^\parallel)^2 + (1 - v^2)|\mathbf{z}_r^\perp|^2} \right). \quad (3.2)$$

When the point-like reflector is positioned at  $\mathbf{z}_r$ , we show the focusing point is located at  $\mathbf{z}_f = \phi_v(\mathbf{z}_r)m$  with  $v = c_s/c_0$  under certain condition in Theorem 3.1. Before diving into the mathematical calculation, we first introduce an orthonormal frame  $\{\hat{\mathbf{g}}_1, \hat{\mathbf{g}}_2, \hat{\mathbf{g}}_3\}$  based on  $\mathbf{z}_f$  as follows:

$$\hat{\mathbf{g}}_1 = \frac{1}{|\mathbf{z}_f|} (\mathbf{z}_{f,3} \hat{\mathbf{e}}_1 - \mathbf{z}_{f,1} \hat{\mathbf{e}}_3), \quad \hat{\mathbf{g}}_2 = \hat{\mathbf{e}}_2, \quad \hat{\mathbf{g}}_3 = \frac{1}{|\mathbf{z}_f|} (\mathbf{z}_{f,1} \hat{\mathbf{e}}_1 + \mathbf{z}_{f,3} \hat{\mathbf{e}}_3). \quad (3.3)$$

We illustrate the three coordinate systems in Figure 2.

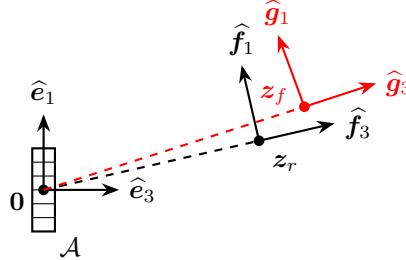


Figure 2: The sensor array and three reference frames  $(\hat{\mathbf{e}}_1, \hat{\mathbf{e}}_3)$ ,  $(\hat{\mathbf{f}}_1, \hat{\mathbf{f}}_3)$ , and  $(\hat{\mathbf{g}}_1, \hat{\mathbf{g}}_3)$ . The unit vector  $\hat{\mathbf{e}}_2 = \hat{\mathbf{f}}_2 = \hat{\mathbf{g}}_2$  are orthogonal to the plane of the figure.

In the case that  $c_s = c_0$ , it is known that the resolution of the image depends on the tilt of the array relative to  $\hat{\mathbf{f}}_3$ , see [6]. In the analysis, we observe that the imaging function also depends on the tilt of the array relative to  $\hat{\mathbf{g}}_3$ . Therefore, for the convenience of presentation, we introduce the cosine of the tilt angles:

$$\alpha_r = \langle \hat{\mathbf{f}}_3, \hat{\mathbf{e}}_3 \rangle = \frac{\mathbf{z}_{r,3}}{|\mathbf{z}_r|}, \quad \alpha_f = \langle \hat{\mathbf{g}}_3, \hat{\mathbf{e}}_3 \rangle = \frac{\mathbf{z}_{f,3}}{|\mathbf{z}_f|}, \quad (3.4)$$

where  $\mathbf{z}_f$  is given by We define the normalized point spread function as

$$\mathcal{G}_{\alpha_r, \alpha_f}(\xi_1, \xi_2, \xi_3, \xi_4) = \frac{1}{|\mathcal{A}_0|} \int_{\mathcal{A}_0} du_1 du_2 \exp \left( -i(\alpha_f u_1 \xi_1 + u_2 \xi_2) - i \frac{u_1^2 \alpha_r^2 + u_2^2}{2} \xi_3 - i \frac{u_1^2 + u_2^2}{2} \xi_4 \right). \quad (3.5)$$

In the theoretical results of the imaging functional,  $\{\xi_j\}$  correspond to different physical meanings.  $\xi_1$  and  $\xi_2$  is related to the transverse direction,  $\xi_3$  corresponds to the range direction and the influence of the wave speed mismatch is reflected through  $\xi_4$ . We observe that the function  $\mathcal{G}_{\alpha_r, \alpha_f}$  is a generalization of the point spread function  $\mathcal{G}_{\alpha_r}$  defined in Section 6, [6]. The two functions have similar qualitative behaviors when  $\xi_3 = 0$  (or  $\xi_4 = 0$ ). When  $\xi_3, \xi_4 \neq 0$ , the behavior of the function  $\mathcal{G}_{\alpha_r, \alpha_f}$  is complicated, which leads to the complicated coupling phenomenon of the range component and the mismatch of the wave speed in the point spread function, which is discussed in 3.2. Figure 3 illustrates the behavior of  $\mathcal{G}_{\alpha_r, \alpha_f}$  through an example.

In the following, we show the asymptotic expression for the generalized imaging function under the regime we consider. Through stationary phase analysis, we quantify the dependence of the imaging functional on the following factors:

- the normalized array radius  $a_0$ ,
- the distance of the reflector to the center of the sensor array  $|\mathbf{z}_r|$ ,
- the central frequency  $\omega_c = \frac{\omega_0}{\varepsilon}$ ,
- the effective bandwidth  $\frac{B_H}{\varepsilon}$ ,

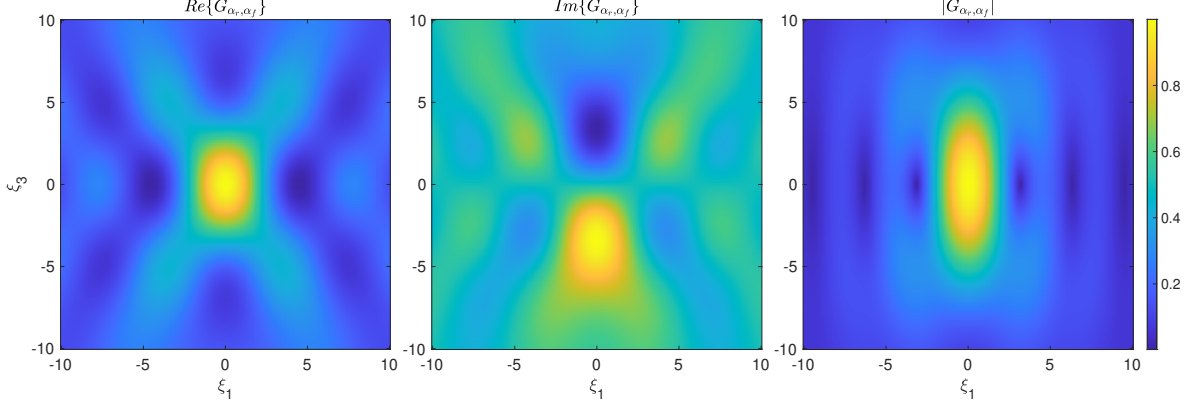


Figure 3: We pick the example that  $\mathbf{z}_r = (-5, 0, 50)$ ,  $v = 1.1$  and calculate  $\alpha_r$  and  $\alpha_f$  according to (3.4) with  $\mathbf{z}_f = \phi_v(\mathbf{z}_r)$ . We plot the function  $\mathcal{G}_{\alpha_r, \alpha_f}(\xi_1, 0, \xi_3, 0)$  showing its real part, imaginary part, and modulus from left to right.

- the chosen speed of sound for migration  $c_s$ .

**Theorem 3.1.** *Let us assume that  $\widehat{F}(\omega)$  has the form*

$$\widehat{F}(\omega) = \frac{1}{B_H} \left( \widehat{F}_0 \left( \frac{\omega_0 - \omega}{B_H} \right) + \widehat{F}_0 \left( \frac{\omega_0 + \omega}{B_H} \right) \right), \quad (3.6)$$

where  $\omega_0, B_H > 0$ . The generalized daylight imaging functional is non-negligible (i.e. it presents a well-defined peak) when the searching wave speed  $c_s$  satisfies

$$v = \frac{c_s}{c_0} \geq 1 - \left( \frac{\mathbf{z}_{r,3}}{|\mathbf{z}_r^\perp|} \right)^2. \quad (3.7)$$

For a given  $c_s$  that satisfying (3.7), as a function of  $\mathbf{z}_s$ , the imaging functional  $\mathcal{I}(\mathbf{z}_s, c_s)$  defined by (2.11) has the focusing point

$$\mathbf{z}_f = \phi_v(\mathbf{z}_r) = \left( v^2 \mathbf{z}_r^\perp, v \sqrt{(\mathbf{z}_r^\parallel)^2 + (1 - v^2) |\mathbf{z}_r^\perp|^2} \right). \quad (3.8)$$

At the searching point  $\mathbf{z}_s$ :

$$\mathbf{z}_s = \mathbf{z}_f + \mathbf{r}_s = \mathbf{z}_f + \varepsilon^{\frac{1}{2}} v^2 \eta_1 \hat{\mathbf{g}}_1 + \varepsilon^{\frac{1}{2}} v^2 \eta_2 \hat{\mathbf{g}}_2 + \varepsilon v \eta_3 \hat{\mathbf{g}}_3, \quad (3.9)$$

the imaging functional has the asymptotic form (as  $\varepsilon \rightarrow 0$ ):

$$\mathcal{I}(\mathbf{z}_s, c_s) \approx \frac{\sigma_r \ell_r^3 N^2}{2^6 \pi^3 c_0 \varepsilon} \frac{\mathcal{K}(\mathbf{0}, \mathbf{z}_r)}{|\mathbf{z}_r|^2} \cdot \mathcal{P}(\mathbf{r}_s, c_s), \quad (3.10)$$

where

$$\mathcal{K}(\mathbf{x}, \mathbf{z}) = \int_0^\infty K \left( \mathbf{x} + \frac{\mathbf{x} - \mathbf{z}}{|\mathbf{x} - \mathbf{z}|} \cdot \mathbf{l} \right) d\mathbf{l}, \quad (3.11)$$

and  $\mathcal{P}(\mathbf{r}_s, c_s)$  is the point spread function defined by

$$\begin{aligned} \mathcal{P}(\mathbf{r}_s, c_s) = & \operatorname{Re} \left\{ \int_{\mathcal{B}} d\omega \left( -i\omega \widehat{F}(\omega) \right) \exp \left( -i \frac{\omega}{c_0} \left( 2\eta_3 + \frac{c_s^2(\eta_1^2 + \eta_2^2)}{c_0^2 |\mathbf{z}_r|} \right) \right) \right. \\ & \times \left. \mathcal{G}_{\alpha_r, \alpha_f}^2 \left( \frac{-a_0 \omega}{c_0 |\mathbf{z}_r|} \eta_1, \frac{-a_0 \omega}{c_0 |\mathbf{z}_r|} \eta_2, 0, \frac{-a_0^2 \omega}{c_0 |\mathbf{z}_r|} \left( \left( \frac{c_0}{c_s} \right)^2 - 1 \right) \right) \right\}. \end{aligned} \quad (3.12)$$

If additionally  $B_H \ll \omega_0$ , then the point spread function has the form

$$\begin{aligned} \mathcal{P}(\mathbf{r}_s, c_s) \simeq & 4\pi\omega_0 \operatorname{Re} \left\{ -i \exp \left( -i \frac{\omega_0}{c_0} \left( 2\eta_3 + \frac{c_s^2(\eta_1^2 + \eta_2^2)}{c_0^2|\mathbf{z}_r|} \right) \right) F_0 \left( -\frac{B_H}{c_0} \left( 2\eta_3 + \frac{c_s^2(\eta_1^2 + \eta_2^2)}{c_0^2|\mathbf{z}_r|} \right) \right) \right. \\ & \left. \times \mathcal{G}_{\alpha_r, \alpha_f}^2 \left( \frac{-a_0\omega_0}{c_0|\mathbf{z}_r|} \eta_1, \frac{-a_0\omega_0}{c_0|\mathbf{z}_r|} \eta_2, 0, \frac{-a_0^2\omega_0}{c_0|\mathbf{z}_r|} \left( \left( \frac{c_0}{c_s} \right)^2 - 1 \right) \right) \right\}, \end{aligned} \quad (3.13)$$

whose slowly varying envelope is given by

$$\begin{aligned} \mathcal{P}_E(\mathbf{r}_s, c_s) \simeq & 2\pi\omega_0 \left| F_0 \left( -\frac{B_H}{c_0} \left( 2\eta_3 + \frac{c_s^2(\eta_1^2 + \eta_2^2)}{c_0^2|\mathbf{z}_r|} \right) \right) \right| \\ & \times \left| \mathcal{G}_{\alpha_r, \alpha_f} \left( \frac{-a_0\omega_0}{c_0|\mathbf{z}_r|} \eta_1, \frac{-a_0\omega_0}{c_0|\mathbf{z}_r|} \eta_2, 0, \frac{-a_0^2\omega_0}{c_0|\mathbf{z}_r|} \left( \left( \frac{c_0}{c_s} \right)^2 - 1 \right) \right) \right|^2. \end{aligned} \quad (3.14)$$

*Proof.* See Appendix A.1.  $\square$

Here, we emphasize that the expression above is valid when the bandwidth of the noise sources is not very small (compared to the order  $\mathcal{O}(\varepsilon)$ ). When the bandwidth is of order  $\mathcal{O}(\varepsilon)$ , the expression of the imaging functional is slightly different from the previous one.

**Proposition 3.2.** *Let us assume that  $\widehat{F}(\omega)$  has the form*

$$\widehat{F}(\omega) = \frac{1}{\varepsilon B_0} \left( \widehat{F}_0 \left( \frac{\omega_0 - \omega}{\varepsilon B_0} \right) + \widehat{F}_0 \left( \frac{\omega_0 + \omega}{\varepsilon B_0} \right) \right), \quad (3.15)$$

where  $\omega_0, B_0 > 0$ . Under the condition (3.7), at the searching point  $\mathbf{z}_s$ :

$$\mathbf{z}_s = \mathbf{z}_f + \mathbf{r}_s = \mathbf{z}_f + \varepsilon^{\frac{1}{2}} v^2 \eta_1 \widehat{\mathbf{g}}_1 + \varepsilon^{\frac{1}{2}} v^2 \eta_2 \widehat{\mathbf{g}}_2 + v \eta_3 \widehat{\mathbf{g}}_3, \quad (3.16)$$

such that  $|\mathbf{r}_s| \ll |\mathbf{z}_r|$ , the imaging functional has the asymptotic form (as  $\varepsilon \rightarrow 0$ ):

$$\mathcal{I}(\mathbf{z}_s, c_s) \approx \frac{\sigma_r \ell_r^3 N^2}{2^6 \pi^3 c_0 \varepsilon} \frac{\mathcal{K}(\mathbf{0}, \mathbf{z}_r)}{|\mathbf{z}_r|^2} \cdot \widetilde{\mathcal{P}}(\mathbf{r}_s, c_s), \quad (3.17)$$

where  $\widetilde{\mathcal{P}}(\mathbf{r}_s, c_s)$  is the point spread function defined by

$$\begin{aligned} \widetilde{\mathcal{P}}(\mathbf{r}_s, c_s) = & 4\pi\omega_0 \operatorname{Re} \left\{ -i \exp \left( -i \frac{\omega_0}{c_0} \left( 2 \frac{\eta_3}{\varepsilon} + \frac{c_s^2(\eta_1^2 + \eta_2^2)}{c_0^2|\mathbf{z}_r|} \right) \right) F_0 \left( -\frac{2B_0\eta_3}{c_0} \right) \right. \\ & \left. \times \mathcal{G}_{\alpha_r, \alpha_f}^2 \left( \frac{-a_0\omega_0}{c_0|\mathbf{z}_r|} \eta_1, \frac{-a_0\omega_0}{c_0|\mathbf{z}_r|} \eta_2, \frac{-a_0^2\omega_0}{c_0|\mathbf{z}_r|^2} \eta_3, \frac{-a_0^2\omega_0}{c_0|\mathbf{z}_r|} \left( \left( \frac{c_0}{c_s} \right)^2 - 1 \right) \right) \right\}. \end{aligned} \quad (3.18)$$

If  $B_0$  is larger than the critical value

$$B_c := \frac{\omega_0}{2} \frac{a_0^2}{|\mathbf{z}_r|^2}, \quad (3.19)$$

then the point spread function has the form

$$\begin{aligned} \widetilde{\mathcal{P}}(\mathbf{r}_s, c_s) = & 4\pi\omega_0 \operatorname{Re} \left\{ -i \exp \left( -i \frac{\omega_0}{c_0} \left( 2 \frac{\eta_3}{\varepsilon} + \frac{c_s^2(\eta_1^2 + \eta_2^2)}{c_0^2|\mathbf{z}_r|} \right) \right) F_0 \left( -\frac{2B_0\eta_3}{c_0} \right) \right. \\ & \left. \times \mathcal{G}_{\alpha_r, \alpha_f}^2 \left( \frac{-a_0\omega_0}{c_0|\mathbf{z}_r|} \eta_1, \frac{-a_0\omega_0}{c_0|\mathbf{z}_r|} \eta_2, 0, \frac{-a_0^2\omega_0}{c_0|\mathbf{z}_r|} \left( \left( \frac{c_0}{c_s} \right)^2 - 1 \right) \right) \right\}, \end{aligned} \quad (3.20)$$

whose slowly varying envelope is given by

$$\mathcal{P}_E(\mathbf{r}_s, c_s) = 2\pi\omega_0 \left| F_0 \left( -\frac{2B_0\eta_3}{c_0} \right) \right| \cdot \left| \mathcal{G}_{\alpha_r, \alpha_f} \left( \frac{-a_0\omega_0}{c_0|\mathbf{z}_r|} \eta_1, \frac{-a_0\omega_0}{c_0|\mathbf{z}_r|} \eta_2, 0, \frac{-a_0^2\omega_0}{c_0|\mathbf{z}_r|} \left( \left( \frac{c_0}{c_s} \right)^2 - 1 \right) \right) \right|^2. \quad (3.21)$$

If  $B_0$  is smaller than the critical value  $B_c$ , then the point spread function has the form

$$\begin{aligned} \tilde{\mathcal{P}}(\mathbf{r}_s, c_s) = & 4\pi\omega_0 \operatorname{Re} \left\{ -i \exp \left( -i \frac{\omega_0}{c_0} \left( 2 \frac{\eta_3}{\varepsilon} + \frac{c_s^2(\eta_1^2 + \eta_2^2)}{c_0^2|\mathbf{z}_r|} \right) \right) F_0(0) \right. \\ & \left. \times \mathcal{G}_{\alpha_r, \alpha_f}^2 \left( \frac{-a_0\omega_0}{c_0|\mathbf{z}_r|} \eta_1, \frac{-a_0\omega_0}{c_0|\mathbf{z}_r|} \eta_2, \frac{-a_0^2\omega_0}{c_0|\mathbf{z}_r|^2} \eta_3, \frac{-a_0^2\omega_0}{c_0|\mathbf{z}_r|} \left( \left( \frac{c_0}{c_s} \right)^2 - 1 \right) \right) \right\}, \end{aligned} \quad (3.22)$$

whose slowly varying envelope is given by

$$\mathcal{P}_E(\mathbf{r}_s, c_s) = 2\pi\omega_0 |F_0(0)| \cdot \left| \mathcal{G}_{\alpha_r, \alpha_f} \left( \frac{-a_0\omega_0}{c_0|\mathbf{z}_r|} \eta_1, \frac{-a_0\omega_0}{c_0|\mathbf{z}_r|} \eta_2, \frac{-a_0^2\omega_0}{c_0|\mathbf{z}_r|^2} \eta_3, \frac{-a_0^2\omega_0}{c_0|\mathbf{z}_r|} \left( \left( \frac{c_0}{c_s} \right)^2 - 1 \right) \right) \right|^2. \quad (3.23)$$

*Proof.* See Appendix A.2.  $\square$

Here, we discuss and interpret the results derived in the theorem and proposition above. For  $c_s = c_0$ , we recover the well-known result for the resolution analysis of the daylight passive imaging configuration. We refer to a more detailed introduction to [6]. For completeness, we summarize the results as follows:

- the frames  $\{\hat{\mathbf{f}}_1, \hat{\mathbf{f}}_2, \hat{\mathbf{f}}_3\}$  and  $\{\hat{\mathbf{g}}_1, \hat{\mathbf{g}}_2, \hat{\mathbf{g}}_3\}$  coincide, and the image is centered at  $\mathbf{z}_r$ ,
- the cross-range resolution is:  $\frac{\lambda|\mathbf{z}_r|}{a\alpha_r}$  in the  $\hat{\mathbf{f}}_1$  direction and  $\frac{\lambda|\mathbf{z}_r|}{a}$  in the  $\hat{\mathbf{f}}_2$  direction,
- the range resolution is  $\frac{\varepsilon c_0}{2B_H}$  in the broadband case ( $\frac{B_H}{\varepsilon} \gg B_c$ ) and  $\frac{\lambda|\mathbf{z}_r|^2}{a^2}$  in the narrowband case ( $\frac{B_H}{\varepsilon} \ll B_c$ ).

The effect caused by the mismatch of  $c_s$  and  $c_0$  can be summarized in the following.

- When the point-like reflector has moderate perpendicular distance to the  $\hat{\mathbf{e}}_3$  axis, i.e, the condition 3.7 is satisfied, the image is not negligible.
- In the broadband case, the image focuses at the point  $\mathbf{z}_f = \phi_v(\mathbf{z}_r)$ . The vectors  $\hat{\mathbf{g}}_1$  and  $\hat{\mathbf{g}}_2$  define the transverse directions of the image, and  $\hat{\mathbf{g}}_3$  defines the range direction. Furthermore, the resolution is the same as described in the case  $c_s = c_0$ .
- In the narrowband case, the mismatch couples with the range direction behavior, which causes further shift of the exact focusing point of the image in the range direction. We illustrate this phenomenon by plotting the function  $|\mathcal{G}_{\alpha_r, \alpha_f}|^2$  for three different choices of  $c_s$  in Figure 4.
- The mismatch causes the reduction of the peak value at the focusing point for all cases except for the narrowband case with  $\alpha_r = 1$ . This fact paves the way for the estimation of  $c_0$  in the general case as discussed in the next section.
- The narrowband case with  $\alpha_r = 1$  is a special case where the range component couples with the mismatch in the following way:

$$\mathcal{P}_E(\mathbf{r}_s, c_s) \sim \left| \mathcal{G}_{\alpha_r, \alpha_f} \left( \frac{-a_0\omega_0}{c_0|\mathbf{z}_r|} \eta_1, \frac{-a_0\omega_0}{c_0|\mathbf{z}_r|} \eta_2, \frac{-a_0^2\omega_0}{c_0|\mathbf{z}_r|^2} \left( \eta_3 + |\mathbf{z}_r| \left( \left( \frac{c_0}{c_s} \right)^2 - 1 \right) \right), 0 \right) \right|^2.$$

This means that along the line defined by  $\eta_1 = \eta_2 = 0$  and  $\eta_3 + |\mathbf{z}_r| \left( \left( \frac{c_0}{c_s} \right)^2 - 1 \right) = 0$ , the point spread function remains at its maximum. Consequently, in this particular case, the peak of the point spread function envelope cannot be used to estimate  $c_0$ . Therefore, this scenario is unfavorable for simultaneously estimating the wave speed and imaging the unknown reflector. However, if either the background speed or the reflector position is known, it is still possible to estimate the remaining unknown parameter.

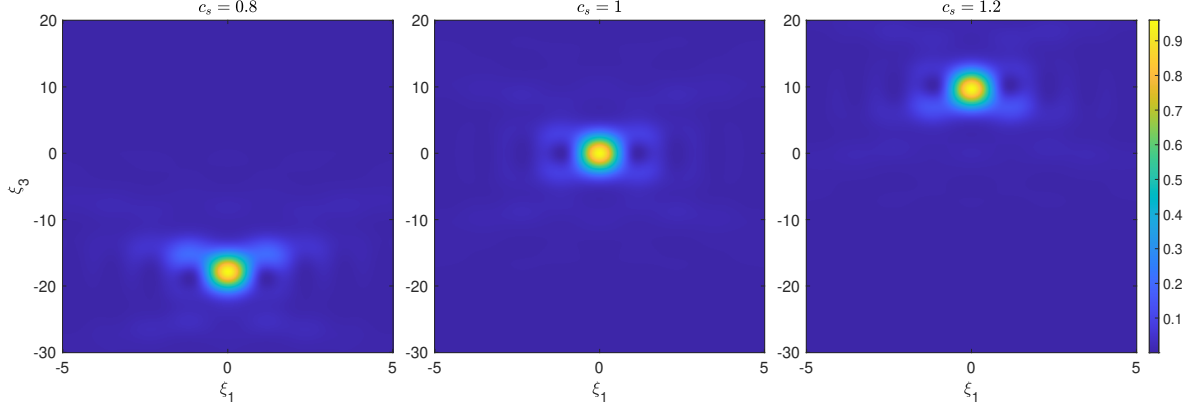


Figure 4: We pick the example that  $a_0 = 20$ ,  $\omega_0 = 4$ ,  $c_0 = 1$ , and  $\mathbf{z}_r = (10, 0, 20\sqrt{2})$ . We plot the profile of  $\left| \mathcal{G}_{\alpha_r, \alpha_f} \left( \frac{-a_0 \omega_0}{c_0 |\mathbf{z}_r|} \eta_1, 0, \frac{-a_0^2 \omega_0}{c_0 |\mathbf{z}_r|^2} \eta_3, \frac{-a_0^2 \omega_0}{c_0 |\mathbf{z}_r|} \left( \left( \frac{c_0}{c_s} \right)^2 - 1 \right) \right) \right|^2$  for three different choices of  $c_s$ :  $c_s = 0.8$  (left),  $c_s = 1$  (middle) and  $c_s = 1.2$  (right). The peaks of the three plots takes value 0.87, 1 and 0.96 respectively.

### 3.2 Estimator for the wave speed

Previously, we have derived the asymptotic expression of the generalized daylight migration imaging functional when there is a mismatch between the chosen wave speed for backpropagation and the true wave speed in the medium. Based on that, we propose the estimators for the position of the reflector and the wave speed  $c_0$  except for the narrowband case with  $\alpha_r = 1$ . We start with the following corollary.

**Corollary 3.3.** *The function  $\mathcal{P}_E$  defined in (3.14), (3.23) and (3.21) achieves its global maximum at  $\mathbf{r}_s = 0$ ,  $c_s = c_0$ .*

*Proof.* We only need to notice that the function  $|\mathcal{G}_{\alpha_r, \alpha_f}(\xi_1, \xi_2, \xi_3, \xi_4)|$  achieves its global maximum at  $\xi_j = 0$ ,  $j = 1, 2, 3, 4$ , and the function  $F_0(\omega)$  achieves its maximum at  $\omega = 0$ .  $\square$

Based on the corollary above, we propose the following estimator:

**Estimator.**

$$(\hat{\mathbf{z}}_r, \hat{c}) = \operatorname{argmax}_{\mathbf{z}_s, c_s} \operatorname{Envelope}\{\mathcal{I}(\mathbf{z}_s, c_s)\}. \quad (3.24)$$

To implement the proposed estimator, we first note that the generalized daylight migration imaging functional does not directly provide its envelope. To extract the envelope, we apply the Hilbert transform to  $\mathcal{I}(\mathbf{z}_s, c_s)$ . Specifically, we discretize the search domain in spherical coordinates. For each fixed pair of angular variables, the Hilbert transform is performed along the radial direction. This process is then repeated to encompass the entire search domain. The corresponding pseudo-code is provided below.

The resolution of the estimator for the reflector is discussed in Section 3.1. Similarly, based on the theoretical results, we observe that the relative resolution for the wave speed estimation is given by  $\frac{\lambda |\mathbf{z}_r|}{a^2}$  for both narrowband and broadband cases. We discuss this result in the following.

- Compared with the relative cross-range resolution of reflector localization, given by  $\frac{\lambda}{a}$ , the relative resolution for wave speed estimation differs by an additional factor of  $|\mathbf{z}_r|/a$  and the cosine of the tilt angle.
- In the narrowband case, the relative resolution for wave speed estimation coincides with the relative range resolution for reflector localization. In contrast, in the broadband case, the relative resolution for wave speed estimation is poorer than the relative range resolution for reflector localization.

---

**Algorithm 1:** Reflector location and wave speed estimation

---

**Input:** Search domain  $\Omega \subset \mathbb{R}^3$ , a searching grid of  $c_s$ , measurement data  $u(t, \mathbf{z}_r)$ .  
**Output:** The estimators  $(\hat{\mathbf{z}}_r, \hat{c})$

- 1 Calculate the cross-correlation;
- 2 Discretize the search domain  $\Omega$  in spherical coordinates  $\{(r_j, \theta_k, \varphi_l)\}$ ;
- 3 **foreach** fixed searching wave speed  $c_s$  **do**
- 4   **foreach** fixed angular pair  $(\theta_k, \varphi_l)$  **do**
- 5     Perform the Hilbert transform of  $\mathcal{I}((r_j, \theta_k, \varphi_l), c_s)$  along the radial variable  $r$ ;
- 6     Store the resulting envelope along the radial direction;
- 7 Assemble the envelopes obtained for all  $(\theta_k, \varphi_l)$  to cover the full search domain;
- 8 Calculate the estimators using (3.24);
- 9 **return** The estimators  $(\hat{\mathbf{z}}_r, \hat{c})$ ;

---

- The relative resolution scales inversely with the Fresnel number, defined as

$$F_{\text{num}} \sim \frac{a^2}{\lambda |\mathbf{z}_r|}.$$

When  $F_{\text{num}} \gg 1$ , the resolution is high, consistent with the geometric optics approximation adopted in the analysis. When  $F_{\text{num}} \lesssim 1$ , diffraction effects become significant, the geometric optics approximation breaks down, and the resolution deteriorates accordingly.

## 4 Effective wave speed estimation through virtual guide star

In this section, we develop a method for estimating the effective wave speed in random media, extending the guide-star strategy introduced earlier. Since a random medium does not contain a physical guide star, we instead introduce a *virtual guide star* at a location of our own choice within the medium. This virtual guide star is not a physical reflector; rather, it is realized indirectly through a family of searching points in the imaging functional. The theoretical principles underlying this construction are presented in Section 4.1, and the corresponding practical estimator is described in Section 4.2.

### 4.1 Probing the speckle

In practice, our goal is to probe a fixed physical location in the medium, denoted by  $\mathbf{z}_g$  and referred to as the *virtual guide star*. The key observation is that a mismatch between the true propagation speed and the backpropagation speed  $c_s$  causes a reflector located at  $\mathbf{z}_r \in \mathcal{D}$  to focus at a shifted location

$$\mathbf{z}_f = \phi_v(\mathbf{z}_r)$$

in the imaging domain. For any fixed  $v$ , the mapping  $\phi_v : \mathbb{R}^3 \rightarrow \mathbb{R}^3$ , defined in (3.2), is bijective.

To probe the medium appropriately, we proceed as follows. For a given backpropagation speed  $c_s$ , we prescribe a travel time  $t_g$  and define the corresponding searching point in the imaging functional as

$$\mathbf{z}_s(c_s, t_g) = (0, 0, c_s \cdot t_g).$$

With this choice, the associated physical location of the virtual guide star is given by

$$\mathbf{z}_g = \phi_v^{-1}(\mathbf{z}_s(c_s, t_g)) = (0, 0, c_0 \cdot t_g),$$

which is independent of  $c_s$ . Therefore, although the searching point  $\mathbf{z}_s$  varies with the assumed backpropagation speed, it always corresponds to the same physical location  $\mathbf{z}_g$  in the medium.

In principle, the virtual guide star can be placed anywhere within the domain  $\mathcal{D}$  by a similar procedure described above. For simplicity, we restrict our attention to locations along the  $\hat{\mathbf{e}}_3$ -axis. This is perfectly

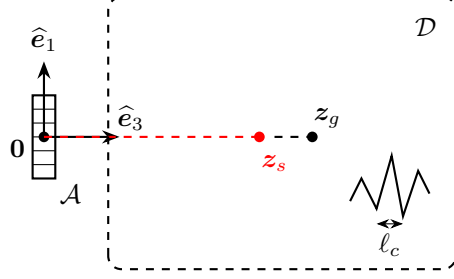


Figure 5: Illustration for the effective wave speed estimation. For any fixed  $c_s$ , we pick the searching point at  $\mathbf{z}_s$ , and the virtual guide star is positioned at  $\mathbf{z}_g = \phi_v^{-1}(\mathbf{z}_s)$  with  $v = c_s/c_0$ .

legitimate as random scatterers are distributed throughout the medium. The corresponding geometric configuration is illustrated in Figure 5.

The following theorem characterizes the behavior of the imaging functional at the searching points associated with the virtual guide star and the packpropagation wave speed.

**Theorem 4.1.** *Let us assume that  $\widehat{F}(\omega)$  has the form*

$$\widehat{F}(\omega) = \frac{1}{B_H} \left( \widehat{F}_0 \left( \frac{\omega_0 - \omega}{B_H} \right) + \widehat{F}_0 \left( \frac{\omega_0 + \omega}{B_H} \right) \right), \quad (4.1)$$

where  $\omega_0, B_H > 0$ . For any fixed  $c_s$  and a prescribed travel time  $t_g$ , choosing the search point

$$\mathbf{z}_s(c_s, t_g) = (0, 0, c_s \cdot t_g)$$

induces a virtual guide star located at

$$\mathbf{z}_g = \phi_v^{-1}(\mathbf{z}_s(c_s, t_g)) = (0, 0, c_0 \cdot t_g),$$

which is independent of  $c_s$ . Denote the vector  $\boldsymbol{\eta} = (\eta_1, \eta_2, \eta_3)$ , and  $\mathbf{r}(\boldsymbol{\eta}) = (\varepsilon^{\frac{1}{2}}\eta_1, \varepsilon^{\frac{1}{2}}\eta_2, \varepsilon\eta_3)$ , then the imaging functional has the asymptotic form (as  $\varepsilon \rightarrow 0$ ):

$$\mathcal{I}(\mathbf{z}_s(c_s, t_g), c_s) \approx \frac{N^2 \varepsilon}{2^6 \pi^3 c_0} \frac{\mathcal{K}(\mathbf{0}, \mathbf{z}_g)}{|\mathbf{z}_g|^2} \cdot \int_{\mathbb{R}^3} \rho_\mu(\mathbf{z}_g(t_g) + \mathbf{r}(\boldsymbol{\eta})) \mathcal{P}_\mu(t_g, \boldsymbol{\eta}, c_s) d\boldsymbol{\eta}, \quad (4.2)$$

where  $\mathcal{P}_\mu(t_g, \boldsymbol{\eta}, c_s)$  is the point spread function defined by

$$\begin{aligned} \mathcal{P}_\mu(t_g, \boldsymbol{\eta}, c_s) = & \operatorname{Re} \left\{ \int_{\mathcal{B}} d\omega \left( -i\omega \widehat{F}(\omega) \right) \exp \left( i \frac{\omega}{c_0} \left( 2\eta_3 + \frac{(\eta_1^2 + \eta_2^2)}{|\mathbf{z}_g|} \right) \right) \right. \\ & \left. \times \mathcal{G}_{1,1}^2 \left( \frac{a_0 \omega}{c_0 |\mathbf{z}_g|} \eta_1, \frac{a_0 \omega}{c_0 |\mathbf{z}_g|} \eta_2, 0, \frac{-a_0^2 \omega}{c_0 |\mathbf{z}_g|} \left( \left( \frac{c_0}{c_s} \right)^2 - 1 \right) \right) \right\}. \end{aligned} \quad (4.3)$$

If additionally  $B_H \ll \omega_0$ , then the point spread function has the form

$$\begin{aligned} \mathcal{P}_\mu(t_g, \boldsymbol{\eta}, c_s) \simeq & 4\pi \omega_0 \operatorname{Re} \left\{ -i \exp \left( i \frac{\omega_0}{c_0} \left( 2\eta_3 + \frac{(\eta_1^2 + \eta_2^2)}{|\mathbf{z}_g|} \right) \right) F_0 \left( \frac{B_H}{c_0} \left( 2\eta_3 + \frac{(\eta_1^2 + \eta_2^2)}{|\mathbf{z}_g|} \right) \right) \right. \\ & \left. \times \mathcal{G}_{1,1}^2 \left( \frac{a_0 \omega_0}{c_0 |\mathbf{z}_g|} \eta_1, \frac{a_0 \omega_0}{c_0 |\mathbf{z}_g|} \eta_2, 0, \frac{-a_0^2 \omega_0}{c_0 |\mathbf{z}_g|} \left( \left( \frac{c_0}{c_s} \right)^2 - 1 \right) \right) \right\}. \end{aligned} \quad (4.4)$$

*Proof.* See Appendix B.1.  $\square$

**Remark 4.2.** In this section, we only consider the case where the bandwidth is not very small compared to the order of the wavelength,  $\mathcal{O}(\varepsilon)$ . We expect that the similar methodology can be extended to the narrowband case as well.

We observe that the mismatch between  $c_s$  and  $c_0$  plays a role in the profile of the point spread function, which is a random quantity that depends on the realization of the random medium  $\rho_\mu$ . The following proposition offers insight that we can extract the information of  $c_0$  from the second-order moment of the imaging functional.

**Proposition 4.3.** (second order moment) *Following the assumptions in Theorem 4.1, we have*

$$\mathbb{E}|\mathcal{I}(\mathbf{z}_s(c_s, t_g), c_s)|^2 \sim \ell_c^3 \|\Sigma\|_{L^1(\mathbb{R}^3)} \cdot \int_{\mathbb{R}^3} |\mathcal{P}_\mu(t_g, \boldsymbol{\eta}, c_s)|^2 d\boldsymbol{\eta}. \quad (4.5)$$

If  $B_H \ll \omega_0$ , we have

$$\begin{aligned} \mathbb{E}|\mathcal{I}(\mathbf{z}_s(c_s, t_g), c_s)|^2 &\sim \int_{\mathbb{R}^3} \left| F_0 \left( \frac{B_H}{c_0} \left( 2\eta_3 + \frac{\eta_1^2 + \eta_2^2}{|\mathbf{z}_g|} \right) \right) \right|^2 \\ &\quad \times \left| \mathcal{G}_{1,1} \left( \frac{a_0 \omega_0}{c_0 |\mathbf{z}_g|} \eta_1, \frac{a_0 \omega_0}{c_0 |\mathbf{z}_g|} \eta_2, 0, \frac{-a_0^2 \omega_0}{c_0 |\mathbf{z}_g|} \left( \left( \frac{c_0}{c_s} \right)^2 - 1 \right) \right) \right|^4 d\eta_1 d\eta_2 d\eta_3. \end{aligned} \quad (4.6)$$

*Proof.* See Appendix B.2.  $\square$

Although the second order moment provides the information of  $c_0$ , we should be aware that we access to only one realization of the random medium in practice. The following two propositions show that by changing the searching point with distance of the order of the wavelength, the imaging functional is stationary, which links the spatial average to the ensemble average.

**Proposition 4.4.** (Locally stationary) *Let  $\Delta \mathbf{z} = (\Delta \mathbf{z}^\perp, \Delta \mathbf{z}^\parallel)$ , and  $\mathbf{p}(\Delta \mathbf{z}, c_s) = \left( \frac{\Delta \mathbf{z}^\perp}{v^2}, \frac{\Delta \mathbf{z}^\parallel}{v} \right)$ , we have*

$$\mathcal{I}(\mathbf{z}_s(c_s, t_g) + \varepsilon \Delta \mathbf{z}, c_s) \simeq \frac{N^2 \varepsilon}{2^6 \pi^3 c_0} \frac{\mathcal{K}(\mathbf{0}, \mathbf{z}_g)}{|\mathbf{z}_g|^2} \cdot \int_{\mathbb{R}^3} \rho_\mu(\mathbf{z}_g + \varepsilon \mathbf{p}(\Delta \mathbf{z}, c_s) + \mathbf{r}(\boldsymbol{\eta})) \mathcal{P}_\mu(t_g, \boldsymbol{\eta}, c_s) d\boldsymbol{\eta}, \quad (4.7)$$

In particular,  $\mathcal{I}$  is stationary in the leading order.

The proof of the proposition is almost the same calculation as the one in Theorem 4.1. Now, we are able to link the spatial and ensemble averages by showing the ergodicity.

**Proposition 4.5.** (spatial average to ensemble average) *Let  $\mathcal{S}(l) = [-\frac{l}{2}, \frac{l}{2}]^3$ , we have*

$$\frac{1}{|\mathcal{S}(l)|} \int_{\mathcal{S}(l)} |\mathcal{I}(\mathbf{z}_s(c_s, t_g) + \varepsilon \Delta \mathbf{z}, c_s)|^2 d\Delta \mathbf{z} \xrightarrow{l \rightarrow \infty} \mathbb{E}|\mathcal{I}(\mathbf{z}_s(c_s, t_g), c_s)|^2 \quad a.s. \quad (4.8)$$

*Proof.* See Appendix B.3.  $\square$

In summary, by calculating the spatial average of  $|\mathcal{I}(\mathbf{z}_s(c_s, t_g) + \varepsilon \Delta \mathbf{z}, c_s)|^2$  for  $\Delta \mathbf{z} \in \mathcal{S}(l)$  with sufficiently large  $l$ , we can approximate the ensemble average  $\mathbb{E}|\mathcal{I}(\mathbf{z}_s(c_s, t_g), c_s)|^2$ , which contains the information of  $c_0$ . Hence, the spatial average can be used to estimate the effective wave speed.

## 4.2 Effective wave speed estimation

In this section, we discuss the procedure of the effective wave speed estimation. We start with the following characterization of the second order moment for the regime  $B_H \ll \omega_0$ .

**Corollary 4.6.** *For  $\mathbb{E}|\mathcal{I}(\mathbf{z}_s(c_s, t_g), c_s)|^2$  given in (4.6), we have*

$$c_0 = \arg \max_{c_s} \mathbb{E}|\mathcal{I}(\mathbf{z}_s(c_s, t_g), c_s)|^2$$

*Proof.* See Appendix B.4.  $\square$

Then, it is straightforward to propose the following estimator for the effective wave speed based on the spatial average of  $\mathcal{I}(\mathbf{z}_s(c_s, t_g) + \Delta \mathbf{z}, c_s)$  as follows:

**Estimator.** For an appropriate choice of  $l > 0$ ,

$$\hat{c}_{\text{eff}} = \operatorname{argmax}_{c_s} \frac{1}{|\mathcal{S}(l)|} \int_{\mathcal{S}(l)} |\mathcal{I}(\mathbf{z}_s(c_s, t_g) + \varepsilon \Delta \mathbf{z}, c_s)|^2 d\Delta \mathbf{z}. \quad (4.9)$$

We summarize the whole procedure of estimating the effective wave speed in the following pseudo-code.

---

**Algorithm 2:** Effective wave speed estimation

---

**Input:** A searching grid of  $c_s$ , a grid for spatial average  $\{\Delta \mathbf{z}_j\}_{j=1}^N$ , an appropriate choice of  $t_g$ , typical wave length in the medium  $\varepsilon$ , measurement data  $u(t, \mathbf{x}_r)$ .

**Output:** The estimator  $\hat{c}_{\text{eff}}$

- 1 Calculate the cross-correlation;
- 2 **foreach** fixed searching wave speed  $c_s$  **do**
- 3   | Calculate the imaging point  $\mathbf{z}_s(c_s, t_g) = (0, 0, c_s t_g)$ ;
- 4   | Calculate the quantity  $I = \frac{1}{N} \sum_j |\mathcal{I}(\mathbf{z}_s(c_s, t_g) + \varepsilon \Delta \mathbf{z}_j)|^2$ ;
- 5 Calculate the estimators using (4.9);
- 6 **return** The estimator  $\hat{c}_{\text{eff}}$ ;

---

Finally, we notice that the formula (4.6) indicates that the realtive resolution of the effective wave speed estimator is given by  $\frac{\lambda |\mathbf{z}_g|}{a^2}$ .

## 5 Numerical experiments

In this section, we present the numerical experiments carried out for the estimators introduced in sections 3-4. All simulations are performed in MATLAB on a machine equipped with an M3 8-core CPU. For reference, the computation time for each numerical experiment is reported. We note that all algorithms can be further accelerated using high-performance GPUs, as the code is primarily based on matrix and tensor operations.

We assume that the available data is the theoretical cross-correlation  $C^{(1)}$  given in (2.9). Owing to the statistical stability of the cross-correlation, one may alternatively start from the raw sensor-array recordings, provided that the recording time window is sufficiently large.

### 5.1 Homogeneous medium with a point reflector

We consider a homogeneous background medium with wave speed  $c_0 = 1$ . The distribution of the noise sources is described by

$$K(\mathbf{x}) = \exp \left[ - \left( \frac{(x_1 + 50)^2}{500} + \frac{(x_2 + 50)^2}{500} + \frac{(x_3 - 42.5)^2}{10} \right) \right].$$

The power spectral density is assumed to be  $\hat{F}(\omega) = \omega^2 e^{-\omega^2}$ . The sensor array lies in the plane  $\operatorname{span}\{\mathbf{e}_1, \mathbf{e}_2\}$  with coordinates  $(5j, 5k, 0)$  for  $j, k = -2, -1, \dots, 2$ . The point reflector is positioned at  $(-5, 0, 50)$  with  $\sigma_r l_r^3 = 0.01$ . The numerical configuration is illustrated in Figure 6.

For generating the synthetic wave data, we employ the domain  $[-50, 50] \times [-50, 50] \times [-50, 35]$  in the  $\{\hat{\mathbf{e}}_1, \hat{\mathbf{e}}_2, \hat{\mathbf{e}}_3\}$  coordinates, discretized into a  $101 \times 101 \times 16$  grid for  $K(\mathbf{x})$ . The frequency range is discretized as  $0 : 5 \times 10^{-3} : 4$ , and the time-lag variable  $\tau$  is sampled on the grid  $40 : 10^{-2} : 300$ . The data-generation stage takes approximately 6.4 minutes.

#### 5.1.1 Localization and wave speed estimation

We choose the imaging window to be a square of side length 30 in the plane  $\operatorname{span}\{\mathbf{e}_1, \mathbf{e}_3\}$ , centered at the reflector, with a grid step size of 0.5. Figure 7 displays the numerical results of the generalized daylight migration imaging functional. We present the cases  $c_s = 0.8$ ,  $c_s = 1$ , and  $c_s = 1.2$ . The black diamond indicates the theoretical focusing location given by (3.8). The total computation time for producing the

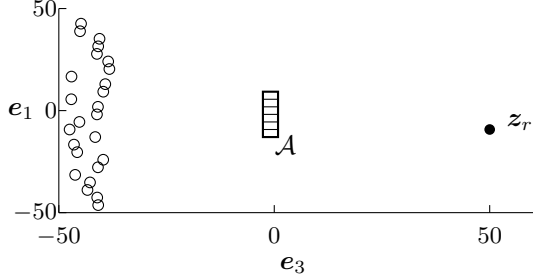


Figure 6: The sensor array is positioned at the center of the plane span{ $e_1, e_2$ }, the reflector is positioned at  $(-5, 0, 50)$ , and the circles on the left represent the source region which is described by  $K(\mathbf{x})$ .

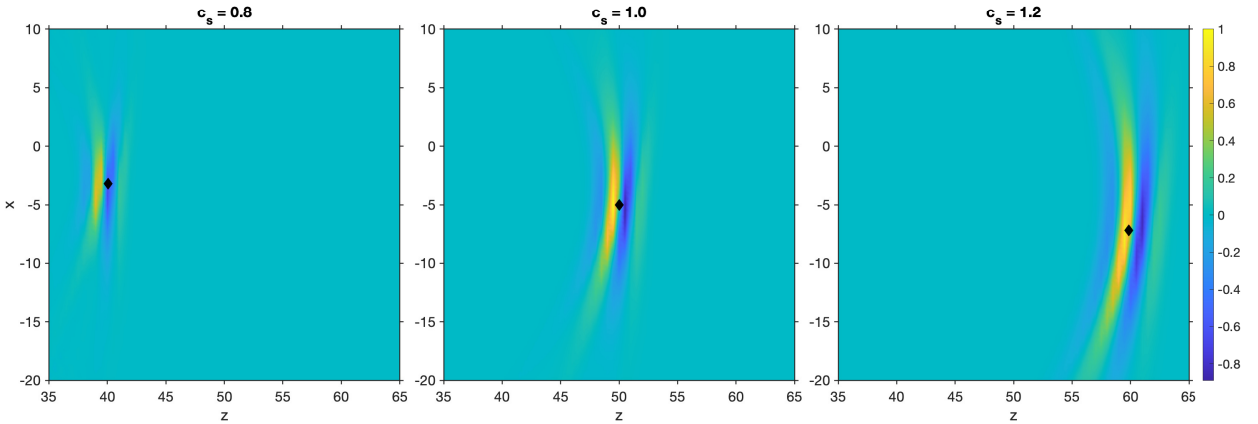


Figure 7: Numerical simulation for different choices of  $c_s$ . The black diamond represents the theoretically predicted focus point of the image,  $\mathbf{z}_f$ . Specifically, the diamond in the middle graph shows the exact position of the reflector.

three images is about 3 seconds. The simulation agrees well with the theoretical prediction, and the shift in the focusing point as  $c_s$  varies is clearly observable.

Next, we conduct numerical experiments to estimate the wave speed. To this end, we consider the profile of the function

$$\phi_1(c_s) := \max_{\mathbf{z}_s} \text{Envelope}\{\mathcal{I}_{\text{num}}(\mathbf{z}_s, c_s)\}, \quad (5.1)$$

obtained from numerical simulations. Here, the imaging functional  $\mathcal{I}_{\text{num}}$  is defined as

$$\mathcal{I}_{\text{num}}(\mathbf{z}_s, c_s) := \frac{N^2}{|\mathcal{A}|^2} \iint_{\mathcal{A}^2} d\mathbf{x}_1 d\mathbf{x}_2 C^{(1)}(\mathcal{T}_s(\mathbf{z}_s, \mathbf{x}_2) + \mathcal{T}_s(\mathbf{z}_s, \mathbf{x}_1), \mathbf{x}_1, \mathbf{x}_2), \quad (5.2)$$

where  $C^{(1)}$  is given in (2.9).

The search domain for  $\mathbf{z}_s$  is discretized in spherical coordinates, with radius ranging from 30 to 70, polar angle from 0 to  $12^\circ$ , and azimuthal angle from  $-8^\circ$  to  $8^\circ$ , using a  $300 \times 80 \times 80$  grid. The wave speed is sampled from 0.7 to 1.3 with step size 0.02. The entire computation takes approximately 3 minutes.

For comparison, we also compute the theoretical prediction

$$\phi_2(c_s) := \text{Envelope}\{\mathcal{P}(0, c_s)\} \simeq \left| \int_0^\infty d\omega \left( -i\omega \widehat{F}(\omega) \right) \mathcal{G}_{\alpha_r, \alpha_f}^2 \left( 0, 0, 0, \frac{-a_0^2 \omega}{c_0 |\mathbf{z}_r|} \left( \left( \frac{c_0}{c_s} \right)^2 - 1 \right) \right) \right|.$$

Figure 8 displays both  $\phi_1(c_s)$  and  $\phi_2(c_s)$ , each appropriately normalized. The theoretical and numerical curves agree well, and the wave speed can be accurately recovered by maximizing  $\phi_1(c_s)$ .

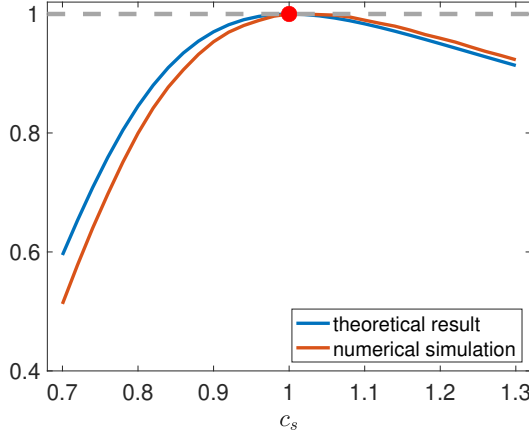


Figure 8: Simulation and theoretical results for the wave speed estimation

Error	Mean	Variance	RMSE
$E_{r,est}$	$3.795 \times 10^{-2}$	$1.517 \times 10^{-4}$	$3.988 \times 10^{-2}$
$E_{r,true}$	$-9.776 \times 10^{-4}$	$3.262 \times 10^{-12}$	$9.776 \times 10^{-4}$
$E_{c,est}$	$2.366 \times 10^{-3}$	$1.050 \times 10^{-6}$	$2.576 \times 10^{-3}$
$E_{c,true}$	$2.241 \times 10^{-3}$	$7.607 \times 10^{-7}$	$2.403 \times 10^{-3}$

Table 1: Mean, variance, and root mean square error (RMSE) of relative range and cross-range localization errors over 100 Monte Carlo trials. All errors are normalized by the true target range.

### 5.1.2 Monte Carlo experiment

We conduct Monte Carlo simulations to assess the statistical stability of the proposed wave-speed estimator in a homogeneous background medium. We consider 100 independent realizations of the noisy sources. For each realization, 500 sampling points are drawn according to the density function  $K(\mathbf{z})$ , and the corresponding cross-correlations are computed. The discretization grid for the wave data generalization is the same as that used in the previous experiments.

For wave-speed estimation, the searching grid for  $c_s$  is chosen as 0.9:0.005:1.1, and the search domain is the same as that used in the previous experiments except for the refinement of the spatial grid in the region of interest to  $500 \times 100 \times 100$ . The statistical results are described in the following. The estimated mean wave speed is 1.0379, the sample variance is  $1.4151 \times 10^{-4}$ , and the root mean square error (RMSE) is 0.0397. The total computational time for the Monte Carlo simulations is approximately 20 hours.

We also evaluate the relative localization errors for the reflector using the estimated wave speed and the true wave speed from each Monte Carlo trial. We denote the estimator using estimated wave speed as  $\hat{\mathbf{z}}_{r,est}$ , and the one using the true wave speed as  $\hat{\mathbf{z}}_{r,true}$ . The relative range and cross-range errors are defined as

$$E_{r,est} = \frac{\langle \hat{\mathbf{z}}_{r,est}, \mathbf{z}_r \rangle}{|\mathbf{z}_r|^2}, \quad E_{c,est} = \frac{\sqrt{|\hat{\mathbf{z}}_{r,est} - \mathbf{z}_r|^2 - E_{r,est}}}{|\mathbf{z}_r|},$$

$$E_{r,true} = \frac{\langle \hat{\mathbf{z}}_{r,true}, \mathbf{z}_r \rangle}{|\mathbf{z}_r|^2}, \quad E_{c,true} = \frac{\sqrt{|\hat{\mathbf{z}}_{r,true} - \mathbf{z}_r|^2 - E_{r,true}}}{|\mathbf{z}_r|}.$$

We display the mean, sample variance, and RMSE of these errors in Table 1. We observe that the localization error in the range direction is impacted by the uncertainty in the estimated wave speed. The localization error in the cross-range direction, however, is not sensitive to the estimated wave speed.

## 5.2 Random medium with $\ell_c \ll \lambda$

In this section, we conduct numerical experiments to validate the methodology for estimating the effective wave speed in a random medium, we plot the profile of  $\mathbb{E}|\mathcal{I}(\mathbf{z}_s(c_s, t_g), c_s)|^2$ , where the point spread function without the narrowband approximation is given by (4.6). The parameters are set as  $a_0 = 10$ ,  $c_0 = 1$ , and  $t_g = 50$ . We choose

$$F_0(t) = e^{-\frac{t^2}{2\sigma^2}} \cos(2\pi\nu_0 t), \quad \nu_0 = 10, \quad \sigma = 0.3,$$

for which the corresponding bandwidth  $B_H$  is close to 1. The resulting theoretical profile is shown in Figure 9, whose peak is attained at  $c_s = c_0 = 1$ .

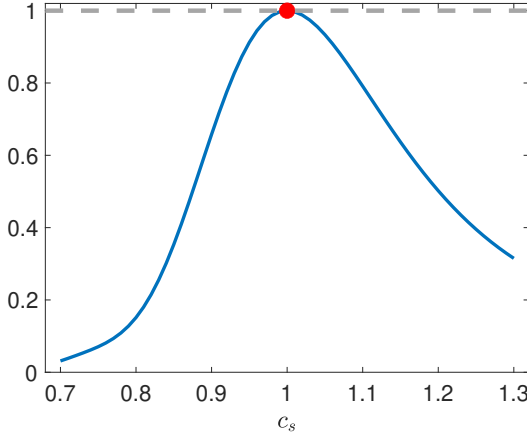


Figure 9: Plot of the profile of  $\mathbb{E}|\mathcal{I}(\mathbf{z}_s(c_s, t_g), c_s)|^2$  given in (4.6). The peak is achieved at  $c_s = c_0 = 1$ .

## 6 Conclusion

In this paper, we investigated passive imaging in the daylight configuration and developed a mathematical framework to quantitatively analyze the impact of wave-speed mismatch in backpropagation-based reflector imaging. When the searching speed matches the true background speed, our results recover the classical resolution analysis for point-reflector imaging. In the presence of mismatch, we derived explicit formulas characterizing both the spatial shift of the reflector and the defocusing of the associated point spread function. This analysis naturally leads to a novel estimator for the background wave speed.

We further extended the framework to random media and introduced the concept of a virtual guide star, which enables an effective and robust wave-speed estimator under daylight illumination. For clarity of exposition and without loss of generality, our analysis focused on the case where the virtual guide star lies on the axis perpendicular to the sensor array.

We expect that the theoretical framework developed here provides a foundation for further advances in wave-speed estimation within the broader field of passive imaging.

## Appendix A Proofs of the results in Section 3

### Appendix A.1 Proof of Theorem 3.1

To begin with, we observe that

$$C^{(1)}(\tau, \mathbf{x}_1, \mathbf{x}_2) = C^{(1)}(-\tau, \mathbf{x}_2, \mathbf{x}_1),$$

we write

$$\mathcal{I}(\mathbf{z}_s, c_s) \approx \mathcal{I}_{\text{I}+}(\mathbf{z}_s, c_s) + \mathcal{I}_{\text{II}+}(\mathbf{z}_s, c_s) + \mathcal{I}_{\text{I}-}(\mathbf{z}_s, c_s) + \mathcal{I}_{\text{II}-}(\mathbf{z}_s, c_s),$$

where

$$\mathcal{I}_{\text{I}\pm}(\mathbf{z}_s, c_s) = \frac{N^2}{2|\mathcal{A}|^2} \iint_{\mathcal{A}^2} d\mathbf{x}_1 d\mathbf{x}_2 C_{\text{I}}^{(1)}(\pm(\mathcal{T}_s(\mathbf{z}_s, \mathbf{x}_2) + \mathcal{T}_s(\mathbf{z}_s, \mathbf{x}_1)), \mathbf{x}_1, \mathbf{x}_2),$$

and

$$\mathcal{I}_{\text{II}\pm}(\mathbf{z}_s, c_s) = \frac{N^2}{2|\mathcal{A}|^2} \iint_{\mathcal{A}^2} d\mathbf{x}_1 d\mathbf{x}_2 C_{\text{II}}^{(1)}(\pm(\mathcal{T}_s(\mathbf{z}_s, \mathbf{x}_2) + \mathcal{T}_s(\mathbf{z}_s, \mathbf{x}_1)), \mathbf{x}_1, \mathbf{x}_2).$$

We first focus on the calculation of  $\mathcal{I}_{\text{I}+}$ . We have

$$C_{\text{I}}^{(1)}(\tau, \mathbf{x}_1, \mathbf{x}_2) = \frac{\sigma_r \ell_r^3}{2^7 \pi^4 c_0^2 \varepsilon^2} \iint d\mathbf{y} d\omega \frac{\omega^2 \widehat{F}(\omega) K(\mathbf{y})}{|\mathbf{x}_2 - \mathbf{z}_r| |\mathbf{z}_r - \mathbf{y}| |\mathbf{x}_1 - \mathbf{y}|} e^{i \frac{\Phi_{\text{I}}(\omega, \mathbf{y})}{\varepsilon}},$$

where

$$\Phi_{\text{I}}(\omega, \mathbf{y}) = \omega(\mathcal{T}(\mathbf{x}_2, \mathbf{y}) + \mathcal{T}(\mathbf{z}_r, \mathbf{y}) - \mathcal{T}(\mathbf{x}_1, \mathbf{y}) - \tau).$$

Therefore, we derive that

$$\mathcal{I}_{\text{I}+}(\mathbf{z}_s, c_s) = \frac{\sigma_r \ell_r^3}{2^8 \pi^4 c_0^2 \varepsilon^2} \frac{N^2}{|\mathcal{A}|^2} \iint_{\mathcal{A}^2} d\sigma(\mathbf{x}_1) d\sigma(\mathbf{x}_2) \iint d\mathbf{y} d\omega \frac{\omega^2 \widehat{F}(\omega) K(\mathbf{y})}{|\mathbf{x}_2 - \mathbf{z}_r| |\mathbf{z}_r - \mathbf{y}| |\mathbf{x}_1 - \mathbf{y}|} e^{i \frac{\Phi_{\text{I}+}(\omega, \mathbf{y}, \mathbf{x}_1, \mathbf{x}_2)}{\varepsilon}}, \quad (\text{A.1})$$

where

$$\Phi_{\text{I}+}(\omega, \mathbf{y}, \mathbf{x}_1, \mathbf{x}_2, \mathbf{z}_s) = \omega(\mathcal{T}(\mathbf{x}_2, \mathbf{z}_r) + \mathcal{T}(\mathbf{z}_r, \mathbf{y}) - \mathcal{T}(\mathbf{x}_1, \mathbf{y}) - \mathcal{T}_s(\mathbf{x}_1, \mathbf{z}_s) - \mathcal{T}_s(\mathbf{x}_2, \mathbf{z}_s))$$

The analysis of the imaging function highly relies on the analysis of the term  $\Phi_{\text{I}+}$ , in the following, we divide the calculation of the (generalized) travel times into two parts.

First, we consider  $\mathcal{T}(\mathbf{x}_2, \mathbf{z}_r) - \mathcal{T}_s(\mathbf{x}_2, \mathbf{z}_s)$ .

Let the searching point be

$$\mathbf{z}_s = \mathbf{z}_f + \varepsilon^{\frac{1}{2}} \mathbf{r},$$

where  $\mathbf{z}_f$  is the focusing point to be determined. By Taylor expansion, we derive

$$\begin{aligned} |\mathbf{z}_r - \mathbf{x}_2| &= |\mathbf{z}_r| - \varepsilon^{\frac{1}{2}} \frac{\langle \mathbf{z}_r, \widetilde{\mathbf{x}_2} \rangle}{|\mathbf{z}_r|} + \mathcal{O}(\varepsilon), \\ |\mathbf{z}_s - \mathbf{x}_2| &= |\mathbf{z}_s| - \varepsilon^{\frac{1}{2}} \frac{\langle \mathbf{z}_s, \widetilde{\mathbf{x}_2} \rangle}{|\mathbf{z}_s|} + \mathcal{O}(\varepsilon) = |\mathbf{z}_f| + \varepsilon^{\frac{1}{2}} \frac{\langle \mathbf{z}_f, \mathbf{r} \rangle}{|\mathbf{z}_f|} - \varepsilon^{\frac{1}{2}} \frac{\langle \mathbf{z}_r, \widetilde{\mathbf{x}_2} \rangle}{|\mathbf{z}_r|} + \mathcal{O}(\varepsilon). \end{aligned}$$

To avoid rapid phase terms in the integral (A.1), we derive

- For  $\mathcal{O}(1)$  terms:  $\frac{|\mathbf{z}_r|}{c_0} = \frac{|\mathbf{z}_f|}{c_s}$ .
- For  $\mathcal{O}(\varepsilon^{\frac{1}{2}})$  terms:  $\frac{\langle \mathbf{z}_f, \mathbf{r} \rangle - \langle \mathbf{z}_f, \widetilde{\mathbf{x}_2} \rangle}{c_s |\mathbf{z}_f|} + \frac{\langle \mathbf{z}_r, \widetilde{\mathbf{x}_2} \rangle}{c_0 |\mathbf{z}_r|} = \frac{\langle \mathbf{z}_f, \mathbf{r} \rangle}{v^2 |\mathbf{z}_r| c_0} + \frac{\langle \mathbf{z}_r - \frac{\mathbf{z}_f}{v^2}, \widetilde{\mathbf{x}_2} \rangle}{c_0 |\mathbf{z}_r|} \sim \mathcal{O}(\varepsilon^{\frac{1}{2}})$  holds for all  $\mathbf{r} \in \mathbb{R}^3$ , and  $\widetilde{\mathbf{x}_2} \in \mathbb{R}^2$ .

The two conditions give the following equations for  $\mathbf{z}_f$ :

$$|\mathbf{z}_f| = v|\mathbf{z}_r|, \quad \mathbf{z}_f^\perp = v^2 \mathbf{z}_r^\perp,$$

whose solution provides the position of  $\mathbf{z}_f$ :

$$\mathbf{z}_f = \left( v^2 \mathbf{z}_r^\perp, v \sqrt{(\mathbf{z}_r^\parallel)^2 + (1 - v^2)|\mathbf{z}_r^\perp|^2} \right), \quad \text{provided by } v \geq 1 - \frac{(\mathbf{z}_r^\parallel)^2}{|\mathbf{z}_r^\perp|^2}.$$

In the following calculation, we denote  $\mathbf{z}_f = (\mathbf{z}_{f,1}, 0, \mathbf{z}_{f,3})$  for simplicity.

Meanwhile, the two conditions above lead us to the following correct scale to proceed the analysis to the profile of imaging function. We consider

$$\mathbf{z}_s = \mathbf{z}_f + \mathbf{r}_s,$$

where

$$\mathbf{r}_s = \varepsilon^{\frac{1}{2}} v^2 \eta_1 \hat{\mathbf{g}}_1 + \varepsilon^{\frac{1}{2}} v^2 \eta_2 \hat{\mathbf{g}}_2 + \varepsilon v \eta_3 \hat{\mathbf{g}}_3.$$

We now proceed to the detailed calculation of  $\mathcal{T}(\mathbf{x}_2, \mathbf{z}_r) - \mathcal{T}_s(\mathbf{x}_2, \mathbf{z}_s)$ . By Taylor's expansion, we get

$$|\mathbf{z}_r - \mathbf{x}_2| \simeq |\mathbf{z}_r| - \varepsilon^{\frac{1}{2}} \frac{\langle \mathbf{z}_r, \widetilde{\mathbf{x}_2} \rangle}{|\mathbf{z}_r|} + \varepsilon \frac{|\mathbf{z}_r|^2 |\widetilde{\mathbf{x}_2}|^2 - \langle \mathbf{z}_r, \widetilde{\mathbf{x}_2} \rangle^2}{2|\mathbf{z}_r|^3 c_0}, \quad (\text{A.2})$$

and

$$\begin{aligned} |\mathbf{z}_s - \mathbf{x}_2| &\simeq |\mathbf{z}_s| - \varepsilon^{\frac{1}{2}} \frac{\langle \mathbf{z}_s, \widetilde{\mathbf{x}_2} \rangle}{|\mathbf{z}_s|} + \varepsilon \frac{|\mathbf{z}_s|^2 |\widetilde{\mathbf{x}_2}|^2 - \langle \mathbf{z}_s, \widetilde{\mathbf{x}_2} \rangle^2}{2|\mathbf{z}_s|^3 c_0} \\ &= v|\mathbf{z}_r| - \varepsilon^{\frac{1}{2}} \frac{v \langle \mathbf{z}_r, \widetilde{\mathbf{x}_2} \rangle}{|\mathbf{z}_r|} \\ &\quad + \frac{\varepsilon}{2v|\mathbf{z}_r|} \left( -2v^2(\eta_1 \langle \widetilde{\mathbf{x}_2}, \hat{\mathbf{g}}_1 \rangle + \eta_2 \langle \widetilde{\mathbf{x}_2}, \hat{\mathbf{g}}_2 \rangle) + |\widetilde{\mathbf{x}_2}|^2 - v^2 \langle \widetilde{\mathbf{x}_2}, \hat{\mathbf{f}}_3 \rangle + 2v^2 |\mathbf{z}_r| \eta_3 + v^4 (\eta_1^2 + \eta_2^2) \right) \end{aligned} \quad (\text{A.3})$$

Hence, we derive that

$$\begin{aligned} \mathcal{T}(\mathbf{x}_2, \mathbf{z}_r) - \mathcal{T}_s(\mathbf{x}_2, \mathbf{z}_s) &\simeq -\varepsilon \frac{\eta_3}{c_0} + \varepsilon \frac{|\widetilde{\mathbf{x}_2}|^2}{2|\mathbf{z}_r|c_0} \left( 1 - \frac{1}{v^2} \right) + \frac{\varepsilon}{|\mathbf{z}_r|c_0} \left( \eta_1 \langle \widetilde{\mathbf{x}_2}, \hat{\mathbf{g}}_1 \rangle + \eta_2 \langle \widetilde{\mathbf{x}_2}, \hat{\mathbf{g}}_2 \rangle - \frac{v^2}{2} (\eta_1^2 + \eta_2^2) \right) \\ &= -\varepsilon \frac{\eta_3}{c_0} + \varepsilon \frac{|\widetilde{\mathbf{x}_2}|^2}{2|\mathbf{z}_r|c_0} \left( 1 - \frac{1}{v^2} \right) + \frac{\varepsilon}{|\mathbf{z}_r|c_0} \left( \frac{\widetilde{\mathbf{x}_{2,1}} \mathbf{z}_{f,3}}{|\mathbf{z}_f|} \eta_1 + \widetilde{\mathbf{x}_{2,2}} \eta_2 - \frac{v^2}{2} (\eta_1^2 + \eta_2^2) \right) \end{aligned} \quad (\text{A.4})$$

Now, we focus on the term  $\mathcal{T}(\mathbf{z}_r, \mathbf{y}) - \mathcal{T}(\mathbf{x}_1, \mathbf{y}) - \mathcal{T}_s(\mathbf{x}_1, \mathbf{z}_s)$ .

For the leading order, we have

$$\mathcal{T}(\mathbf{z}_r, \mathbf{y}) - \mathcal{T}(\mathbf{x}_1, \mathbf{y}) - \mathcal{T}_s(\mathbf{x}_1, \mathbf{z}_s) \simeq \frac{|\mathbf{z}_r - \mathbf{y}|}{c_0} - \frac{|\mathbf{y}|}{c_0} - \frac{|\mathbf{z}_s|}{c_s} = \frac{|\mathbf{z}_r - \mathbf{y}| - |\mathbf{y}| - |\mathbf{z}_s|}{c_0}.$$

To avoid the quick phase term in the integral (A.1), we parametrize  $\mathbf{y}$  as follows:

$$\mathbf{y} = |\mathbf{z}_r| \left( -s_3 \hat{\mathbf{f}}_3 + \varepsilon^{\frac{1}{2}} s_1 \hat{\mathbf{f}}_1 + \varepsilon^{\frac{1}{2}} s_2 \hat{\mathbf{f}}_2 \right).$$

The calculation of  $|\mathbf{z}_s - \mathbf{x}_1|$  is similar to (A.3), and we calculate that

$$|\mathbf{z}_r - \mathbf{y}| \simeq |\mathbf{z}_r| \left( (1 + s_3) + \varepsilon \frac{s_1^2 + s_2^2}{2(1 + s_3)} \right), \quad (\text{A.5})$$

and

$$\begin{aligned}
|\mathbf{x}_1 - \mathbf{y}| &\simeq |\mathbf{z}_r| s_3 + \varepsilon^{\frac{1}{2}} \left\langle \widetilde{\mathbf{x}_1}, \widehat{\mathbf{f}}_3 \right\rangle \\
&+ \varepsilon \left( -\frac{\left\langle \widetilde{\mathbf{x}_1}, \widehat{\mathbf{f}}_3 \right\rangle^2}{2|\mathbf{z}_r| s_3} + \frac{1}{2|\mathbf{z}_r| s_3} \left( |\widetilde{\mathbf{x}_1}|^2 + |\mathbf{z}_r|^2 (s_1^2 + s_2^2) - 2|\mathbf{z}_r| \left( s_1 \left\langle \widetilde{\mathbf{x}_1}, \widehat{\mathbf{f}}_1 \right\rangle + s_2 \left\langle \widetilde{\mathbf{x}_1}, \widehat{\mathbf{f}}_2 \right\rangle \right) \right) \right)
\end{aligned} \quad (\text{A.6})$$

Then, we derive that

$$\begin{aligned}
\mathcal{T}(\mathbf{z}_r, \mathbf{y}) - \mathcal{T}(\mathbf{x}_1, \mathbf{y}) - \mathcal{T}_s(\mathbf{x}_1, \mathbf{z}_s) &\simeq -\varepsilon \frac{\eta_3}{c_0} - \varepsilon \frac{v^2(\eta_1^2 + \eta_2^2)}{2|\mathbf{z}_r| c_0} - \varepsilon \frac{|\mathbf{z}_r|}{c_0} \frac{s_1^2 + s_2^2}{2s_3(1 + s_3)} + \varepsilon \frac{\left\langle \widetilde{\mathbf{x}_1}, \mathbf{z}_r \right\rangle^2}{2|\mathbf{z}_r|^3 c_0} \left( 1 + \frac{1}{s_3} \right) \\
&- \varepsilon \frac{|\widetilde{\mathbf{x}_1}|^2}{2|\mathbf{z}_r| c_0} \left( \frac{1}{s_3} + \frac{1}{v^2} \right) + \varepsilon \frac{s_1 \left\langle \widetilde{\mathbf{x}_1}, \widehat{\mathbf{f}}_1 \right\rangle + s_2 \left\langle \widetilde{\mathbf{x}_1}, \widehat{\mathbf{f}}_2 \right\rangle}{c_0 s_3} + \varepsilon \frac{\eta_1 \left\langle \widetilde{\mathbf{x}_1}, \widehat{\mathbf{g}}_1 \right\rangle + \eta_2 \left\langle \widetilde{\mathbf{x}_1}, \widehat{\mathbf{g}}_2 \right\rangle}{|\mathbf{z}_r| c_0} \\
&= -\varepsilon \frac{\eta_3}{c_0} - \varepsilon \frac{v^2(\eta_1^2 + \eta_2^2)}{2|\mathbf{z}_r| c_0} - \varepsilon \frac{|\mathbf{z}_r|}{c_0} \frac{s_1^2 + s_2^2}{2s_3(1 + s_3)} + \varepsilon \frac{s_1}{c_0 s_3} \frac{\mathbf{z}_{r,3}}{|\mathbf{z}_r|} \widetilde{\mathbf{x}_{1,1}} + \varepsilon \frac{s_2}{c_0 s_3} \widetilde{\mathbf{x}_{1,2}} + \varepsilon \frac{\widetilde{\mathbf{x}_{1,1}} \mathbf{z}_{f,3}}{c_0 |\mathbf{z}_r| |\mathbf{z}_f|} \eta_1 + \varepsilon \frac{\widetilde{\mathbf{x}_{1,2}}}{|\mathbf{z}_r| c_0} \eta_2 \\
&+ \varepsilon \frac{\widetilde{\mathbf{x}_{1,1}}^2 z_{r,1}^2}{2c_0 |\mathbf{z}_r|^3} \left( 1 + \frac{1}{s_3} \right) - \varepsilon \frac{|\widetilde{\mathbf{x}_1}|^2}{2c_0 |\mathbf{z}_r|} \left( \frac{1}{s_3} + \frac{1}{v^2} \right)
\end{aligned} \quad (\text{A.7})$$

We compute the integrals in  $s_1$  and  $s_2$

$$\begin{aligned}
&\iint ds_1 ds_2 \exp \left( i \frac{\omega}{\varepsilon} (\mathcal{T}(\mathbf{z}_r, \mathbf{y}) - \mathcal{T}(\mathbf{x}_1, \mathbf{y}) - \mathcal{T}_s(\mathbf{x}_1, \mathbf{z}_s)) \right) \\
&\simeq -\frac{2\pi i c_0 s_3 (1 + s_3)}{\omega |\mathbf{z}_r|} \exp \left( i \frac{\omega}{c_0} \left( \frac{|\widetilde{\mathbf{x}_1}|^2}{2|\mathbf{z}_r|} \left( 1 - \frac{1}{v^2} \right) - \eta_3 - \frac{v^2(\eta_1^2 + \eta_2^2)}{2|\mathbf{z}_r| c_0} + \frac{\widetilde{\mathbf{x}_{1,1}} \mathbf{z}_{f,3}}{|\mathbf{z}_f| |\mathbf{z}_r|} \eta_1 + \frac{\widetilde{\mathbf{x}_{1,2}}}{|\mathbf{z}_r|} \eta_2 \right) \right).
\end{aligned}$$

It gives

$$\begin{aligned}
&\iint ds_1 ds_2 \Phi_{\text{I}+}(\omega, \mathbf{y}, \mathbf{x}_1, \mathbf{x}_2, \mathbf{z}_s) \simeq -\frac{2\pi i c_0 s_3 (1 + s_3)}{\omega |\mathbf{z}_r|} \\
&\times \exp \left( i \frac{\omega}{c_0} \left( \frac{|\widetilde{\mathbf{x}_1}|^2 + |\widetilde{\mathbf{x}_2}|^2}{2|\mathbf{z}_r|} \left( 1 - \frac{1}{v^2} \right) - 2\eta_3 - \frac{v^2(\eta_1^2 + \eta_2^2)}{|\mathbf{z}_r|} + \frac{\mathbf{z}_{f,3} \eta_1}{|\mathbf{z}_f| |\mathbf{z}_r|} (\widetilde{\mathbf{x}_{1,1}} + \widetilde{\mathbf{x}_{2,1}}) + \frac{\eta_2}{|\mathbf{z}_r|} (\widetilde{\mathbf{x}_{1,2}} + \widetilde{\mathbf{x}_{2,2}}) \right) \right).
\end{aligned}$$

Therefore, we obtain

$$\begin{aligned}
\mathcal{I}_{\text{I}+}(\mathbf{z}_s, c_s) &= \frac{\sigma_r \ell_r^3 N^2 \mathcal{K}(\mathbf{0}, \mathbf{z}_r)}{2^6 \pi^3 c_0 |\mathbf{z}_r|^2 \varepsilon} \int_{\mathcal{B}} d\omega \left( -i\omega \widehat{F}(\omega) \right) \exp \left( -i \frac{\omega}{c_0} \left( 2\eta_3 + \frac{c_s^2 (\eta_1^2 + \eta_2^2)}{c_0^2 |\mathbf{z}_r|} \right) \right) \\
&\times \mathcal{G}_{\alpha_r, \alpha_f}^2 \left( \frac{-a_0 \omega}{c_0 |\mathbf{z}_r|} \eta_1, \frac{-a_0 \omega}{c_0 |\mathbf{z}_r|} \eta_2, 0, \frac{-a_0^2 \omega}{c_0 |\mathbf{z}_r|} \left( \left( \frac{c_0}{c_s} \right)^2 - 1 \right) \right)
\end{aligned}$$

Similar calculation can be done for  $\mathcal{I}_{\text{II}+}$ ,  $\mathcal{I}_{\text{I}-}$ , and  $\mathcal{I}_{\text{II}-}$ . Only  $\mathcal{I}_{\text{II}-}$  provides non-vanishing contribution. Hence, the expression in (3.10) is derived.

## Appendix A.2 Proof of Proposition 3.2

We revise the parametrization of the searching point as

$$\mathbf{z}_s = \mathbf{z}_f + \varepsilon^{\frac{1}{2}} v^2 \eta_1 \widehat{\mathbf{g}}_1 + \varepsilon^{\frac{1}{2}} v^2 \eta_2 \widehat{\mathbf{g}}_2 + v \eta_3 \widehat{\mathbf{g}}_3.$$

Compared to the previous one, the scaling in direction  $\widehat{\mathbf{g}}_3$  is changed. We conduct a similar calculation and get

$$\begin{aligned}
|\mathbf{z}_s - \mathbf{x}_2| &\simeq |\mathbf{z}_s| - \varepsilon^{\frac{1}{2}} \frac{\langle \mathbf{z}_s, \widetilde{\mathbf{x}_2} \rangle}{|\mathbf{z}_s|} + \varepsilon \frac{|\mathbf{z}_s|^2 |\widetilde{\mathbf{x}_2}|^2 - \langle \mathbf{z}_s, \widetilde{\mathbf{x}_2} \rangle^2}{2|\mathbf{z}_s|^3 c_0} \\
&= |\mathbf{z}_f| + v\eta_3 - \varepsilon^{\frac{1}{2}} \langle \widetilde{\mathbf{x}_2}, \widehat{\mathbf{g}}_3 \rangle \\
&\quad + \varepsilon \left( \frac{v^4(\eta_1^2 + \eta_2^2)}{2(|\mathbf{z}_f| + v\eta_3)} - \frac{v^2(\eta_1 \langle \widetilde{\mathbf{x}_2}, \widehat{\mathbf{g}}_1 \rangle + \eta_2 \langle \widetilde{\mathbf{x}_2}, \widehat{\mathbf{g}}_2 \rangle)}{|\mathbf{z}_f| + v\eta_3} + \frac{|\widetilde{\mathbf{x}_2}|^2 - \langle \widetilde{\mathbf{x}_2}, \widehat{\mathbf{g}}_3 \rangle^2}{2(|\mathbf{z}_f| + v\eta_3)} \right)
\end{aligned} \tag{A.8}$$

Then, we have

$$\begin{aligned}
\mathcal{T}(\mathbf{x}_2, \mathbf{z}_r) - \mathcal{T}_s(\mathbf{x}_2, \mathbf{z}_s) &\simeq -\frac{\eta_3}{c_0} + \frac{\varepsilon}{c_0} \left( \frac{|\widetilde{\mathbf{x}_2}|^2}{2|\mathbf{z}_r|} - \frac{|\widetilde{\mathbf{x}_2}|^2}{2v(|\mathbf{z}_f| + v\eta_3|)} + \frac{\langle \widetilde{\mathbf{x}_2}, \widehat{\mathbf{g}}_3 \rangle^2}{2v(|\mathbf{z}_f| + v\eta_3|)} - \frac{\langle \widetilde{\mathbf{x}_2}, \widehat{\mathbf{f}}_3 \rangle^2}{2|\mathbf{z}_r|} \right. \\
&\quad \left. + \frac{v(\eta_1 \langle \widetilde{\mathbf{x}_2}, \widehat{\mathbf{g}}_1 \rangle + \eta_2 \langle \widetilde{\mathbf{x}_2}, \widehat{\mathbf{g}}_2 \rangle)}{|\mathbf{z}_f| + v\eta_3} - \frac{v^3(\eta_1^2 + \eta_2^2)}{2(|\mathbf{z}_f| + v\eta_3)} \right) \\
&= -\frac{\eta_3}{c_0} + \frac{\varepsilon}{c_0} \left( \frac{|\widetilde{\mathbf{x}_2}|^2}{2} \left( \frac{1}{|\mathbf{z}_r|} - \frac{1}{v^2(|\mathbf{z}_r| + \eta_3)} \right) + \frac{\widetilde{\mathbf{x}_{2,1}}^2 z_{r,1}^2}{2} \left( \frac{1}{|\mathbf{z}_r| + \eta_3} - \frac{1}{|\mathbf{z}_r|} \right) \right. \\
&\quad \left. - \frac{\widetilde{\mathbf{x}_{2,1}}}{|\mathbf{z}_r| + \eta_3} \frac{z_{f,3}}{|\mathbf{z}_f|} \eta_1 + \frac{\widetilde{\mathbf{x}_{2,2}}}{|\mathbf{z}_r| + \eta_3} \eta_2 - \frac{v^2(\eta_1^2 + \eta_2^2)}{2(|\mathbf{z}_r| + \eta_3)} \right),
\end{aligned} \tag{A.9}$$

and

$$\begin{aligned}
\mathcal{T}(\mathbf{z}_r, \mathbf{y}) - \mathcal{T}(\mathbf{x}_1, \mathbf{y}) - \mathcal{T}_s(\mathbf{x}_1, \mathbf{z}_s) &\simeq -\frac{\eta_3}{c_0} + \frac{\varepsilon}{c_0} \left( -\frac{(s_1^2 + s_2^2)|\mathbf{z}_r|}{2s_3(1 + s_3)} + \frac{\widetilde{\mathbf{x}_{1,1}}^2 z_{r,1}^2}{2} \left( \frac{1}{s_3|\mathbf{z}_r|} + \frac{1}{|\mathbf{z}_r| + \eta_3} \right) \right. \\
&\quad \left. - \frac{|\widetilde{\mathbf{x}_1}|^2}{2} \left( \frac{1}{|\mathbf{z}_r|s_3} + \frac{1}{v^2(|\mathbf{z}_r| + \eta_3)} \right) + \frac{s_1}{s_3} \frac{\mathbf{z}_{r,3}}{\mathbf{z}_r} \widetilde{\mathbf{x}_{1,1}} + \frac{s_2}{s_3} \widetilde{\mathbf{x}_{1,2}} - \frac{v^2(\eta_1^2 + \eta_2^2)}{2(|\mathbf{z}_r| + \eta_3)} + \frac{\mathbf{z}_{f,3}}{|\mathbf{z}_f|} \frac{\widetilde{\mathbf{x}_{1,1}} \eta_1}{|\mathbf{z}_r| + \eta_3} + \frac{\widetilde{\mathbf{x}_{1,2}} \eta_2}{|\mathbf{z}_r| + \eta_3} \right)
\end{aligned} \tag{A.10}$$

Computing the integral in  $s_1$  and  $s_2$ , we derive

$$\begin{aligned}
&\iint ds_1 ds_2 \exp \left( i \frac{\omega}{\varepsilon} (\mathcal{T}(\mathbf{z}_r, \mathbf{y}) - \mathcal{T}(\mathbf{x}_1, \mathbf{y}) - \mathcal{T}_s(\mathbf{x}_1, \mathbf{z}_s)) \right) \\
&\simeq -\frac{2\pi i c_0 s_3 (1 + s_3)}{\omega |\mathbf{z}_r|} \exp \left( i \frac{\omega}{c_0} \left( -2 \frac{\eta_3}{\varepsilon} - \frac{v^2(\eta_1^2 + \eta_2^2)}{|\mathbf{z}_r| + \eta_3} + \varphi(\widetilde{\mathbf{x}_1}) + \varphi(\widetilde{\mathbf{x}_2}) \right) \right),
\end{aligned}$$

where, for  $\mathbf{x} = (x_1, x_2) \in \mathbb{R}^2$ ,  $\varphi(\mathbf{x})$  is defined by

$$\varphi(\mathbf{x}) = \frac{\mathbf{z}_{f,3}}{|\mathbf{z}_f|} \frac{x_1 \eta_1}{|\mathbf{z}_r| + \eta_3} + \frac{x_2 \eta_2}{|\mathbf{z}_r| + \eta_3} + \left( \frac{x_1^2}{2} \frac{\mathbf{z}_{r,3}^2}{|\mathbf{z}_r|^2} + \frac{x_2^2}{2} \right) \frac{\eta_3}{|\mathbf{z}_r|(|\mathbf{z}_r| + \eta_3)} + \frac{|\mathbf{x}|^2}{2} \frac{1 - \frac{1}{v^2}}{|\mathbf{z}_r| + \eta_3}. \tag{A.11}$$

Therefore, we have

$$\begin{aligned}
\mathcal{I}_{+}(\mathbf{z}_s, c_s) &= \frac{\sigma_r \ell_r^3 N^2 \mathcal{K}(\mathbf{0}, \mathbf{z}_r)}{2^6 \pi^3 c_0 |\mathbf{z}_r|^2 \varepsilon} \int_{\mathcal{B}} d\omega \left( -i\omega \widehat{F}(\omega) \right) \exp \left( -i \frac{\omega}{c_0} \left( 2 \frac{\eta_3}{\varepsilon} + \frac{c_s^2(\eta_1^2 + \eta_2^2)}{c_0^2(|\mathbf{z}_r| + \eta_3)} \right) \right) \\
&\quad \times \mathcal{G}_{\alpha_r, \alpha_f}^2 \left( \frac{-a_0 \omega}{c_0(|\mathbf{z}_r| + \eta_3)} \eta_1, \frac{-a_0 \omega}{c_0(|\mathbf{z}_r| + \eta_3)} \eta_2, \frac{-a_0^2 \omega}{c_0 |\mathbf{z}_r|(|\mathbf{z}_r| + \eta_3)} \eta_3, \frac{-a_0^2 \omega}{c_0(|\mathbf{z}_r| + \eta_3)} \left( \left( \frac{c_0}{c_s} \right)^2 - 1 \right) \right)
\end{aligned}$$

Similar calculation can be done for  $\mathcal{I}_{\text{II}+}$ ,  $\mathcal{I}_{\text{I}-}$ , and  $\mathcal{I}_{\text{II}-}$ . Only  $\mathcal{I}_{\text{II}-}$  provides non-vanishing contribution. Hence, we have

$$\begin{aligned}
\mathcal{I}(\mathbf{z}_s, c_s) &\approx \frac{\sigma_r \ell_r^3 N^2 \mathcal{K}(\mathbf{0}, \mathbf{z}_r)}{2^6 \pi^3 c_0 |\mathbf{z}_r|^2 \varepsilon} \text{Re} \left\{ \int_{\mathcal{B}} d\omega \left( -i\omega \widehat{F}(\omega) \right) \exp \left( -i \frac{\omega}{c_0} \left( 2 \frac{\eta_3}{\varepsilon} + \frac{c_s^2(\eta_1^2 + \eta_2^2)}{c_0^2(|\mathbf{z}_r| + \eta_3)} \right) \right) \right. \\
&\quad \left. \times \mathcal{G}_{\alpha_r, \alpha_f}^2 \left( \frac{-a_0 \omega}{c_0(|\mathbf{z}_r| + \eta_3)} \eta_1, \frac{-a_0 \omega}{c_0(|\mathbf{z}_r| + \eta_3)} \eta_2, \frac{-a_0^2 \omega}{c_0 |\mathbf{z}_r|(|\mathbf{z}_r| + \eta_3)} \eta_3, \frac{-a_0^2 \omega}{c_0(|\mathbf{z}_r| + \eta_3)} \left( \left( \frac{c_0}{c_s} \right)^2 - 1 \right) \right) \right\}
\end{aligned} \tag{A.12}$$

Further, by the assumption that the bandwidth is of the order  $\mathcal{O}(\varepsilon)$ :

$$\widehat{F}(\omega) = \frac{1}{\varepsilon B_H} \left( \widehat{F}_0 \left( \frac{\omega_0 - \omega}{\varepsilon B_H} \right) + \widehat{F}_0 \left( \frac{\omega_0 + \omega}{\varepsilon B_H} \right) \right),$$

we derive the following expression

$$\begin{aligned} \mathcal{I}(\mathbf{z}_s, c_s) \approx & \frac{\sigma_r \ell_r^3 N^2 \mathcal{K}(\mathbf{0}, \mathbf{z}_r) \omega_0 \varepsilon}{2^4 \pi^2 c_0 |\mathbf{z}_r|^2} \operatorname{Re} \left\{ -i \exp \left( -i \frac{\omega}{c_0} \left( 2 \frac{\eta_3}{\varepsilon} + \frac{c_s^2 (\eta_1^2 + \eta_2^2)}{c_0^2 (|\mathbf{z}_r| + \eta_3)} \right) \right) F_0 \left( -\frac{2 B_0 \eta_3}{c_0} \right) \right. \\ & \left. \times \mathcal{G}_{\alpha_r, \alpha_f}^2 \left( \frac{-a_0 \omega}{c_0 (|\mathbf{z}_r| + \eta_3)} \eta_1, \frac{-a_0 \omega}{c_0 (|\mathbf{z}_r| + \eta_3)} \eta_2, \frac{-a_0^2 \omega}{c_0 |\mathbf{z}_r| (|\mathbf{z}_r| + \eta_3)} \eta_3, \frac{-a_0^2 \omega}{c_0 (|\mathbf{z}_r| + \eta_3)} \left( \left( \frac{c_0}{c_s} \right)^2 - 1 \right) \right) \right\} \end{aligned} \quad (\text{A.13})$$

The condition that  $|\mathbf{r}_s| \ll |\mathbf{z}_r|$  gives the expression (3.18). When  $B_0 \ll B_c$ , we get the expression (3.22). When  $B_0 \gg B_c$ , we get the expression (3.20).

## Appendix B Proofs of the results in Section 4

### Appendix B.1 Proof of Theorem 4.1

Similar to the proof of Theorem 3.1, we observe that

$$C^{(1)}(\tau, \mathbf{x}_1, \mathbf{x}_2) = C^{(1)}(-\tau, \mathbf{x}_2, \mathbf{x}_1),$$

we write

$$\mathcal{I}(\mathbf{z}_s, c_s) \approx \mathcal{I}_{\text{I}+}(\mathbf{z}_s, c_s) + \mathcal{I}_{\text{II}+}(\mathbf{z}_s, c_s) + \mathcal{I}_{\text{I}-}(\mathbf{z}_s, c_s) + \mathcal{I}_{\text{II}-}(\mathbf{z}_s, c_s),$$

where

$$\mathcal{I}_{\text{I}\pm}(\mathbf{z}_s, c_s) = \frac{N^2}{2|\mathcal{A}|^2} \iint_{\mathcal{A}^2} d\mathbf{x}_1 d\mathbf{x}_2 C_{\text{I}}^{(1)} (\pm(\mathcal{T}_s(\mathbf{z}_s, \mathbf{x}_2) + \mathcal{T}_s(\mathbf{z}_s, \mathbf{x}_1)), \mathbf{x}_1, \mathbf{x}_2),$$

and

$$\mathcal{I}_{\text{II}\pm}(\mathbf{z}_s, c_s) = \frac{N^2}{2|\mathcal{A}|^2} \iint_{\mathcal{A}^2} d\mathbf{x}_1 d\mathbf{x}_2 C_{\text{II}}^{(1)} (\pm(\mathcal{T}_s(\mathbf{z}_s, \mathbf{x}_2) + \mathcal{T}_s(\mathbf{z}_s, \mathbf{x}_1)), \mathbf{x}_1, \mathbf{x}_2).$$

We first focus on the calculation of  $\mathcal{I}_{\text{I}+}$ . We have

$$C_{\text{I}}^{(1)}(\tau, \mathbf{x}_1, \mathbf{x}_2) = \frac{1}{2^7 \pi^4 c_0^2 \varepsilon^2} \int_{\mathcal{D}} dz \rho_{\mu}(z) \iint d\mathbf{y} d\omega \frac{\omega^2 \widehat{F}(\omega) K(\mathbf{y})}{|\mathbf{x}_2 - z| |\mathbf{z} - \mathbf{y}| |\mathbf{x}_1 - \mathbf{y}|} e^{i \frac{\Phi_{\text{I}}(\omega, \mathbf{y}, \mathbf{z})}{\varepsilon}},$$

where

$$\Phi_{\text{I}}(\omega, \mathbf{z}, \mathbf{y}) = \omega(\mathcal{T}(\mathbf{x}_2, \mathbf{y}) + \mathcal{T}(\mathbf{z}, \mathbf{y}) - \mathcal{T}(\mathbf{x}_1, \mathbf{y}) - \tau).$$

Therefore, we derive that

$$\mathcal{I}_{\text{I}+}(\mathbf{z}_s, c_s) = \frac{1}{2^8 \pi^4 c_0^2 \varepsilon^2} \frac{N^2}{|\mathcal{A}|^2} \iint_{\mathcal{A}^2} d\sigma(\mathbf{x}_1) \sigma(\mathbf{x}_2) \int_{\mathcal{D}} \rho_{\mu}(z) dz \iint d\mathbf{y} d\omega \frac{\omega^2 \widehat{F}(\omega) K(\mathbf{y}) e^{i \frac{\Phi_{\text{I}+}(\omega, \mathbf{y}, \mathbf{x}_1, \mathbf{x}_2, \mathbf{z}_s, \mathbf{z})}{\varepsilon}}}{|\mathbf{x}_2 - z| |\mathbf{z} - \mathbf{y}| |\mathbf{x}_1 - \mathbf{y}|}, \quad (\text{B.1})$$

where

$$\Phi_{\text{I}+}(\omega, \mathbf{y}, \mathbf{x}_1, \mathbf{x}_2, \mathbf{z}_s, \mathbf{z}) = \omega(\mathcal{T}(\mathbf{x}_2, \mathbf{z}) + \mathcal{T}(\mathbf{z}, \mathbf{y}) - \mathcal{T}(\mathbf{x}_1, \mathbf{y}) - \mathcal{T}_s(\mathbf{x}_1, \mathbf{z}_s) - \mathcal{T}_s(\mathbf{x}_2, \mathbf{z}_s))$$

The analysis of the imaging function highly relies on the analysis of the term  $\Phi_{\text{I}+}$ , in the following, we divide the calculation of the (generalized) travel times into two parts.

First, we consider  $\mathcal{T}(\mathbf{x}_2, \mathbf{z}) - \mathcal{T}_s(\mathbf{x}_2, \mathbf{z}_s)$ :

By Taylor expansion, we have

$$|\mathbf{x}_2 - \mathbf{z}_s| \simeq |\mathbf{z}_s| + \frac{|\widetilde{\mathbf{x}}_2|^2}{2|\mathbf{z}_s|} \varepsilon, \quad (\text{B.2})$$

and

$$|\mathbf{x}_2 - \mathbf{z}| \simeq |\mathbf{z}_g| + \frac{\varepsilon}{2|\mathbf{z}_g|} (\eta_1^2 + \eta_2^2 + 2\eta_3|\mathbf{z}_g| + |\widetilde{\mathbf{x}}_2|^2 - 2(\eta_1 \langle \widehat{\mathbf{e}}_1, \widetilde{\mathbf{x}}_2 \rangle + \eta_2 \langle \widehat{\mathbf{e}}_2, \widetilde{\mathbf{x}}_2 \rangle)) \quad (\text{B.3})$$

Then, we have

$$\mathcal{T}(\mathbf{x}_2, \mathbf{z}) - \mathcal{T}_s(\mathbf{x}_2, \mathbf{z}_s) \simeq \frac{\varepsilon}{c_0} \left( \frac{\eta_1^2 + \eta_2^2}{2|\mathbf{z}_g|} + \eta_3 + \frac{|\widetilde{\mathbf{x}}_2|^2}{2|\mathbf{z}_g|} \left( 1 - \frac{1}{v^2} \right) - \frac{1}{|\mathbf{z}_g|} (\eta_1 \langle \widehat{\mathbf{e}}_1, \widetilde{\mathbf{x}}_2 \rangle + \eta_2 \langle \widehat{\mathbf{e}}_2, \widetilde{\mathbf{x}}_2 \rangle) \right) \quad (\text{B.4})$$

To calculate the term  $\mathcal{T}(\mathbf{z}, \mathbf{y}) - \mathcal{T}(\mathbf{x}_1, \mathbf{y}) - \mathcal{T}_s(\mathbf{x}_1, \mathbf{z}_s)$ , we introduce the parametrization of  $\mathbf{y}$  as:

$$\mathbf{y} = |\mathbf{z}_g| \left( -s_3 \widehat{\mathbf{e}}_3 + \varepsilon^{\frac{1}{2}} s_1 \widehat{\mathbf{e}}_1 + \varepsilon^{\frac{1}{2}} s_2 \widehat{\mathbf{e}}_2 \right).$$

By Taylor expansion, we have

$$|\mathbf{x}_1 - \mathbf{z}_s| \simeq |\mathbf{z}_s| + \frac{|\widetilde{\mathbf{x}}_1|^2}{2|\mathbf{z}_s|} \varepsilon, \quad (\text{B.5})$$

$$|\mathbf{z} - \mathbf{y}| \simeq (1 + s_3)|\mathbf{z}_g| + \frac{\varepsilon}{2(1 + s_3)|\mathbf{z}_g|} (2\eta_3(1 + s_3|\mathbf{z}_g|) + (\eta_1 - \mathbf{z}_g s_1)^2 + (\eta_2 - \mathbf{z}_g s_2)^2), \quad (\text{B.6})$$

$$|\mathbf{x}_1 - \mathbf{y}| \simeq |\mathbf{z}_g| s_3 + \varepsilon \left( \frac{|\widetilde{\mathbf{x}}_1|^2}{2|\mathbf{z}_g| s_3} + \frac{(s_1^2 + s_2^2)|\mathbf{z}_g|}{2s_3} - \frac{s_1 \langle \widetilde{\mathbf{x}}_1, \widehat{\mathbf{e}}_1 \rangle + s_2 \langle \widetilde{\mathbf{x}}_1, \widehat{\mathbf{e}}_2 \rangle}{s_3} \right). \quad (\text{B.7})$$

Hence, we have

$$\begin{aligned} \mathcal{T}(\mathbf{z}, \mathbf{y}) - \mathcal{T}(\mathbf{x}_1, \mathbf{y}) - \mathcal{T}_s(\mathbf{x}_1, \mathbf{z}_s) &\simeq \frac{\varepsilon}{c_0} \left( -\frac{|\widetilde{\mathbf{x}}_1|^2}{2|\mathbf{z}_g|} \left( \frac{1}{v^2} + \frac{1}{s_3} \right) - \frac{(s_1^2 + s_2^2)|\mathbf{z}_g|}{2s_3} + \frac{s_1 \langle \widetilde{\mathbf{x}}_1, \widehat{\mathbf{e}}_1 \rangle + s_2 \langle \widetilde{\mathbf{x}}_1, \widehat{\mathbf{e}}_2 \rangle}{s_3} \right. \\ &\quad \left. + \eta_3 + \frac{1}{2(1 + s_3)|\mathbf{z}_g|} (|\mathbf{z}_g|^2(s_1^2 + s_2^2) - 2|\mathbf{z}_g|(s_1\eta_1 + s_2\eta_2) + (\eta_1^2 + \eta_2^2)) \right). \end{aligned} \quad (\text{B.8})$$

Computing the integral in  $s_1$  and  $s_2$ , we derive

$$\begin{aligned} &\iint ds_1 ds_2 \exp \left( i \frac{\omega}{\varepsilon} (\mathcal{T}(\mathbf{z}, \mathbf{y}) - \mathcal{T}(\mathbf{x}_1, \mathbf{y}) - \mathcal{T}_s(\mathbf{x}_1, \mathbf{z}_s)) \right) \\ &\simeq -\frac{2\pi i c_0 s_3 (1 + s_3)}{\omega |\mathbf{z}_g|} \exp \left( i \frac{\omega}{c_0} \left( 2\eta_3 + \frac{\eta_1^2 + \eta_2^2}{|\mathbf{z}_g|} + \psi(\widetilde{\mathbf{x}}_1) + \psi(\widetilde{\mathbf{x}}_2) \right) \right), \end{aligned}$$

where, for  $\mathbf{x} = (x_1, x_2) \in \mathbb{R}^2$ ,  $\varphi(\mathbf{x})$  is defined by

$$\psi(\mathbf{x}) = \frac{|\mathbf{x}|^2}{2|\mathbf{z}_g|} \left( 1 - \frac{1}{v^2} \right) - \frac{\eta_1 x_1 + \eta_2 x_2}{|\mathbf{z}_g|}. \quad (\text{B.9})$$

Therefore, we obtain

$$\begin{aligned} \mathcal{I}_{\text{I}+}(\mathbf{z}_s, c_s) &= \frac{N^2 \mathcal{K}(\mathbf{0}, \mathbf{z}_g) \varepsilon}{2^6 \pi^3 c_0 |\mathbf{z}_g|^2} \int \rho_\mu(\mathbf{z}_g(t_g) + \mathbf{r}(\boldsymbol{\eta})) \int_{\mathcal{B}} d\omega \left( -i\omega \widehat{F}(\omega) \right) \exp \left( i \frac{\omega}{c_0} \left( 2\eta_3 + \frac{(\eta_1^2 + \eta_2^2)}{|\mathbf{z}_g|} \right) \right) \\ &\quad \times \mathcal{G}_{1,1}^2 \left( \frac{a_0 \omega}{c_0 |\mathbf{z}_g|} \eta_1, \frac{a_0 \omega}{c_0 |\mathbf{z}_g|} \eta_2, 0, \frac{-a_0^2 \omega}{c_0 |\mathbf{z}_g|} \left( \left( \frac{c_0}{c_s} \right)^2 - 1 \right) \right) d\boldsymbol{\eta}. \end{aligned}$$

Similar calculation can be done for  $\mathcal{I}_{\text{II}+}$ ,  $\mathcal{I}_{\text{I}-}$ , and  $\mathcal{I}_{\text{II}-}$ . Only  $\mathcal{I}_{\text{II}-}$  provides non-vanishing contribution. Hence, we have

$$\begin{aligned} \mathcal{I}(\mathbf{z}_s, c_s) &= \frac{N^2 \mathcal{K}(\mathbf{0}, \mathbf{z}_g) \varepsilon}{2^6 \pi^3 c_0 |\mathbf{z}_g|^2} \int \rho_\mu(\mathbf{z}_g(t_g) + \mathbf{r}(\boldsymbol{\eta})) \operatorname{Re} \left\{ \int_{\mathcal{B}} d\omega \left( -i\omega \widehat{F}(\omega) \right) \exp \left( i \frac{\omega}{c_0} \left( 2\eta_3 + \frac{(\eta_1^2 + \eta_2^2)}{|\mathbf{z}_g|} \right) \right) \right. \\ &\quad \left. \times \mathcal{G}_{1,1}^2 \left( \frac{a_0 \omega}{c_0 |\mathbf{z}_g|} \eta_1, \frac{a_0 \omega}{c_0 |\mathbf{z}_g|} \eta_2, 0, \frac{-a_0^2 \omega}{c_0 |\mathbf{z}_g|} \left( \left( \frac{c_0}{c_s} \right)^2 - 1 \right) \right) \right\} d\boldsymbol{\eta}. \end{aligned}$$

## Appendix B.2 Proof of Proposition 4.3

We observe that

$$\begin{aligned}
\mathbb{E} |\mathcal{I}(\mathbf{z}_s, c_s)|^2 &\sim \int_{\mathcal{D}} \int_{\mathcal{D}} \mathbb{E}(\rho_\mu(\mathbf{z}) \rho_\mu(\mathbf{z}')) \cdot \mathcal{P}(\mathbf{z}, \mathbf{z}_s, c_s) \overline{\mathcal{P}}(\mathbf{z}', \mathbf{z}_s, c_s) d\mathbf{z} d\mathbf{z}' \\
&= \int_{\mathcal{D}} \int_{\mathcal{D}} \Sigma \left( \frac{\mathbf{z} - \mathbf{z}'}{\ell_c} \right) \cdot \mathcal{P}(\mathbf{z}, \mathbf{z}_s, c_s) \overline{\mathcal{P}}(\mathbf{z}', \mathbf{z}_s, c_s) d\mathbf{z} d\mathbf{z}' \\
&= \ell_c^3 \cdot \int_{\mathcal{D}} \int_{\mathcal{D}} \Sigma(\mathbf{x}) \cdot \mathcal{P}(\mathbf{z}' + \ell_c \mathbf{x}, \mathbf{z}_s, c_s) \overline{\mathcal{P}}(\mathbf{z}', \mathbf{z}_s, c_s) d\mathbf{x} d\mathbf{z}' \\
&\simeq l^3 \|\Sigma\|_{L^1(\mathcal{D})} \cdot \int_{\mathbb{R}^3} |\mathcal{P}(\mathbf{z}, \mathbf{z}_s, c_s)|^2 d\mathbf{z},
\end{aligned}$$

where we use Lemma C.1 in the last inequality.

To calculate the profile of the point spread function for  $B_H \ll \omega_0$ , we first denote

$$\phi(\boldsymbol{\eta}) = \frac{1}{c_0} \left( 2\eta_3 + \frac{\eta_1^2 + \eta_2^2}{|\mathbf{z}_g|} \right), \quad \mathcal{G}(\boldsymbol{\eta}) = \mathcal{G}_{1,1} \left( \frac{a_0 \omega_0}{c_0 |\mathbf{z}_g|} \eta_1, \frac{a_0 \omega_0}{c_0 |\mathbf{z}_g|} \eta_2, 0, \frac{-a_0^2 \omega_0}{c_0 |\mathbf{z}_g|} \left( \left( \frac{c_0}{c_s} \right)^2 - 1 \right) \right),$$

and

$$f(\boldsymbol{\eta}) = -i \exp(i\omega_0 \phi(\boldsymbol{\eta})) F_0(B_H \phi(\boldsymbol{\eta})) \cdot \mathcal{G}^2(\boldsymbol{\eta})$$

Then, we notice that

$$\int_{\mathbb{R}^3} |\mathcal{P}_\mu(t_g, \boldsymbol{\eta}, c_s)|^2 d\boldsymbol{\eta} = \frac{1}{2} \int_{\mathbb{R}^3} |f(\boldsymbol{\eta})|^2 d\boldsymbol{\eta} + \frac{1}{2} \operatorname{Re} \left\{ \int_{\mathbb{R}^3} f^2(\boldsymbol{\eta}) d\boldsymbol{\eta} \right\} \triangleq I_1 + I_2. \quad (\text{B.10})$$

For  $I_1$ , we have

$$I_1 = \frac{1}{2} \int_{\mathbb{R}^3} |F_0(B_H \phi(\boldsymbol{\eta}))|^2 |\mathcal{G}(\boldsymbol{\eta})|^4 d\boldsymbol{\eta}.$$

For  $I_2$ , we notice that

$$\frac{\partial}{\partial \eta_3} \phi(\boldsymbol{\eta}) = \frac{2}{c_0}. \quad (\text{B.11})$$

For any fixed  $(\eta_1, \eta_2)$ , we let  $\zeta = B_H \phi(\boldsymbol{\eta})$  and implement the change of variable. We calculate that

$$\eta_3 := \Psi(\eta_1, \eta_2, \zeta) = \frac{c_0}{2} \left( \frac{\zeta}{B_H} - \frac{\eta_1^2 + \eta_2^2}{|\mathbf{z}_g|} \right), \quad (\text{B.12})$$

and the Jacobian is

$$\frac{\partial \eta_3}{\partial \zeta} = \frac{c_0}{2B_H}.$$

Then, we derive that

$$\int_{\mathbb{R}^3} f^2(\boldsymbol{\eta}) d\boldsymbol{\eta} = -\frac{c_0}{2B_H} \int_{\mathbb{R}^2} d\eta_1 d\eta_2 \int_{\mathbb{R}} e^{i \frac{2\omega_0}{B_H} \zeta} F_{H,0}^2(\zeta) \mathcal{G}^4(\eta_1, \eta_2, \zeta) d\zeta$$

Due to the existence of the quick phase term, the integral is negligible. Therefore, we have

$$\begin{aligned}
&\int_{\mathbb{R}^3} |\mathcal{P}_\mu(t_g, \boldsymbol{\eta}, c_s)|^2 d\boldsymbol{\eta} \\
&\simeq \frac{1}{2} \int_{\mathbb{R}^3} \left| F_0 \left( \frac{B_H}{c_0} \left( 2\eta_3 + \frac{\eta_1^2 + \eta_2^2}{|\mathbf{z}_g|} \right) \right) \right|^2 \left| \mathcal{G}_{1,1} \left( \frac{a_0 \omega_0}{c_0 |\mathbf{z}_g|} \eta_1, \frac{a_0 \omega_0}{c_0 |\mathbf{z}_g|} \eta_2, 0, \frac{-a_0^2 \omega_0}{c_0 |\mathbf{z}_g|} \left( \left( \frac{c_0}{c_s} \right)^2 - 1 \right) \right) \right|^4 d\eta_1 d\eta_2 d\eta_3.
\end{aligned}$$

### Appendix B.3 Proof of Proposition 4.5

Here, we provide a proof for the case  $\rho_\mu$  is a stationary Gaussian process. For general stationary process, the proof can be done by a variance calculation.

We notice that the covariance function of the stationary Gaussian process  $\rho_\mu$  is  $L^1$ , then  $\rho_\mu$  is ergodic. Therefore  $|\mathcal{I}(\mathbf{z}_s, c_s)|^2$  is also ergodic as a measurable function of  $\rho_\mu$ . Combined with the stationarity shown in the previous proposition, by Birkhoff's Theorem, we derive the result.

### Appendix B.4 Proof of Corollary 4.6

Here, we offer a qualitative argument. We notice that for fixed  $c_s$ , the essential support  $\mathcal{G}_{1,1}$  concentrates around  $\boldsymbol{\eta} = 0$ , and also the essential support of  $F_0$  concentrate around 0. The quantity  $\mathbb{E}|\mathcal{I}(\mathbf{z}_s, c_s)|^2$  behaves qualitatively as the function  $\left| \mathcal{G}_{1,1} \left( 0, 0, 0, \frac{-a_0^2 \omega_0}{c_0 |\mathbf{z}_s|} \left( \left( \frac{c_0}{c_s} \right)^2 - 1 \right) \right) \right|^4$  up to some multiplicity constant. Then, it is clear that the maximum is achieved at  $c_s = c_0$ .

## Appendix C Auxiliary lemmas

**Lemma C.1.** *For any deterministic function  $f \in \mathcal{C}^1(D)$ ,  $g \in \mathcal{C}^0(D)$ ,*

$$\int_{D \times D} \text{Cov}(n_\varepsilon(\mathbf{x}), n_\varepsilon(\mathbf{y})) f(\mathbf{x}) \overline{g(\mathbf{y})} d\mathbf{x} d\mathbf{y} = \left( \int_{\mathbb{R}^d} \varepsilon^d \Sigma(\mathbf{z}) d\mathbf{z} \right) \cdot \int_D f(\mathbf{x}) \overline{g(\mathbf{x})} d\mathbf{x} + \mathcal{O}(\varepsilon^{d+1})$$

*Proof.* By definition and by a change of variable

$$\begin{aligned} \int_{D \times D} \text{Cov}(n_\varepsilon(\mathbf{x}), n_\varepsilon(\mathbf{y})) f(\mathbf{x}) \overline{g(\mathbf{y})} d\mathbf{x} d\mathbf{y} &= \int_{D \times D} \Sigma \left( \frac{\mathbf{x} - \mathbf{y}}{\varepsilon} \right) f(\mathbf{x}) \overline{g(\mathbf{y})} d\mathbf{x} d\mathbf{y} \\ &= \varepsilon^d \int_D \left( \int_{\frac{D}{\varepsilon}} \Sigma(\mathbf{z}) f(\varepsilon \mathbf{z} + \mathbf{y}) d\mathbf{z} \right) \bar{g}(\mathbf{y}) d\mathbf{y} \end{aligned}$$

Therefore,

$$\begin{aligned} &\left| \int_{D \times D} \text{Cov}(n_\varepsilon(\mathbf{x}), n_\varepsilon(\mathbf{y})) f(\mathbf{x}) \overline{g(\mathbf{y})} d\mathbf{x} d\mathbf{y} - \left( \varepsilon^d \int_{\frac{D}{\varepsilon}} \Sigma(\mathbf{z}) d\mathbf{z} \right) \int_D f(\mathbf{x}) \overline{g(\mathbf{x})} d\mathbf{x} \right| \\ &\lesssim \varepsilon^d \int_{\frac{D}{\varepsilon}} \left( \int_D |g(\mathbf{y})| |f(\varepsilon \mathbf{z} + \mathbf{y}) - f(\mathbf{y})| d\mathbf{y} \right) |\Sigma(\mathbf{z})| d\mathbf{z} \\ &\lesssim \varepsilon^{d+1} \left( \int_{\frac{D}{\varepsilon}} |\Sigma(\mathbf{z})| |\mathbf{z}| d\mathbf{z} \right) \left( \int_D |\nabla f(\mathbf{y})| |g(\mathbf{y})| d\mathbf{y} \right) \end{aligned} \tag{C.1}$$

Since  $\Sigma$  has the decaying rate  $|\Sigma(\mathbf{x})| \lesssim (1 + |\mathbf{x}|)^{-4-\eta}$ , for some  $\eta > 0$ , the right-hand side of the difference converges, which leads to the result.  $\square$

**Lemma C.2.** *We present an integral which is frequently used in the calculation of the point spread function:*

$$\int_{\mathbb{R}} e^{i(-Ax^2 + Bx)} dx = \sqrt{\frac{\pi}{A}} e^{-i\frac{\pi}{4}} e^{i\frac{B^2}{4A}}. \tag{C.2}$$

*Proof.*

$$\int_{\mathbb{R}} e^{i(-Ax^2 + Bx)} dx = \int_{\mathbb{R}} e^{-iA(x - \frac{B}{2A})^2} \cdot e^{i\frac{B^2}{4A}} dx = \sqrt{\frac{\pi}{A}} e^{-i\frac{\pi}{4}} e^{i\frac{B^2}{4A}}, \tag{C.3}$$

where we use the identity that

$$\int_{\mathbb{R}} e^{-i\frac{s^2}{2}} ds = \sqrt{2\pi} e^{-i\frac{\pi}{4}}.$$

$\square$

## References

- [1] R. L. Weaver and O. I. Lobkis, "Ultrasonics without a source: Thermal fluctuation correlations at mhz frequencies," *Physical Review Letters*, vol. 87, no. 13, p. 134301, 2001.
- [2] T. L. Duvall Jr, S. Jefferies, J. Harvey, and M. Pomerantz, "Time-distance helioseismology," *Nature*, vol. 362, no. 6419, pp. 430–432, 1993.
- [3] K. G. Sabra, P. Roux, P. Gerstoft, W. Kuperman, and M. C. Fehler, "Extracting coherent coda arrivals from cross-correlations of long period seismic waves during the mount st. helens 2004 eruption," *Geophysical research letters*, vol. 33, no. 6, 2006.
- [4] A. Curtis, P. Gerstoft, H. Sato, R. Snieder, and K. Wapenaar, "Seismic interferometry—turning noise into signal," *The Leading Edge*, vol. 25, no. 9, pp. 1082–1092, 2006.
- [5] E. Larose, L. Margerin, A. Derode, *et al.*, "Correlation of random wavefields: An interdisciplinary review," *Geophysics*, vol. 71, no. 4, SI11–SI21, 2006.
- [6] J. Garnier and G. Papanicolaou, *Passive Imaging with Ambient Noise*. Cambridge University Press, 2016.
- [7] O. I. Lobkis and R. L. Weaver, "On the emergence of the green's function in the correlations of a diffuse field," *The Journal of the Acoustical Society of America*, vol. 110, no. 6, pp. 3011–3017, 2001.
- [8] R. Snieder, "Extracting the green's function from the correlation of coda waves: A derivation based on stationary phase," *Phys. Rev. E*, vol. 69, p. 046610, 4 Apr. 2004. DOI: 10.1103/PhysRevE.69.046610. [Online]. Available: <https://link.aps.org/doi/10.1103/PhysRevE.69.046610>.
- [9] Y. C. De Verdière, "Semiclassical analysis and passive imaging," *Nonlinearity*, vol. 22, no. 6, R45, 2009.
- [10] C. Bardos, J. Garnier, and G. Papanicolaou, "Identification of green's functions singularities by cross correlation of noisy signals," *Inverse Problems*, vol. 24, no. 1, p. 015011, Jan. 2008. DOI: 10.1088/0266-5611/24/1/015011. [Online]. Available: <https://doi.org/10.1088/0266-5611/24/1/015011>.
- [11] J. Garnier and G. Papanicolaou, "Passive sensor imaging using cross correlations of noisy signals in a scattering medium," *SIAM Journal on Imaging Sciences*, vol. 2, no. 2, pp. 396–437, 2009. DOI: 10.1137/080723454. eprint: <https://doi.org/10.1137/080723454>. [Online]. Available: <https://doi.org/10.1137/080723454>.
- [12] T. Helin, M. Lassas, L. Oksanen, and T. Saksala, "Correlation based passive imaging with a white noise source," *Journal de Mathématiques Pures et Appliquées*, vol. 116, pp. 132–160, 2018, ISSN: 0021-7824. DOI: <https://doi.org/10.1016/j.matpur.2018.05.001>. [Online]. Available: <https://www.sciencedirect.com/science/article/pii/S0021782418300710>.
- [13] A. Agaltsov, T. Hohage, and R. Novikov, "Global uniqueness in a passive inverse problem of helioseismology," *Inverse Problems*, vol. 36, no. 5, p. 055004, 2020.
- [14] A. Bakulin and R. Calvert, "The virtual source method: Theory and case study," *Geophysics*, vol. 71, no. 4, SI139–SI150, 2006.
- [15] K. Wapenaar and J. Thorbecke, "Virtual sources and their responses, part i: Time-reversal acoustics and seismic interferometry," *Geophysical Prospecting*, vol. 65, no. 6, pp. 1411–1429, 2017.
- [16] K. Wapenaar, J. Thorbecke, J. van der Neut, E. Slob, and R. Snieder, "Review paper: Virtual sources and their responses, part ii: Data-driven single-sided focusing," *Geophysical Prospecting*, vol. 65, no. 6, pp. 1430–1451, 2017. DOI: <https://doi.org/10.1111/1365-2478.12495>. eprint: <https://onlinelibrary.wiley.com/doi/pdf/10.1111/1365-2478.12495>. [Online]. Available: <https://onlinelibrary.wiley.com/doi/abs/10.1111/1365-2478.12495>.
- [17] J. Garnier and G. Papanicolaou, "Role of scattering in virtual source array imaging," *SIAM Journal on Imaging Sciences*, vol. 7, no. 2, pp. 1210–1236, 2014.
- [18] P. Gouédard, L. Stehly, F. Brenguier, *et al.*, "Cross-correlation of random fields: Mathematical approach and applications," *Geophysical Prospecting*, vol. 56, no. 3, pp. 375–393, 2008. DOI: <https://doi.org/10.1111/j.1365-2478.2007.00684.x>. eprint: <https://onlinelibrary.wiley.com/doi/pdf/10.1111/j.1365-2478.2007.00684.x>. [Online]. Available: <https://onlinelibrary.wiley.com/doi/abs/10.1111/j.1365-2478.2007.00684.x>.

[19] U. Harmankaya, A. Kaslilar, J. Thorbecke, K. Wapenaar, and D. Draganov, “Locating near-surface scatterers using non-physical scattered waves resulting from seismic interferometry,” *Journal of Applied Geophysics*, vol. 91, pp. 66–81, 2013.

[20] A. Kaslilar, U. Harmankaya, K. Wapenaar, and D. Draganov, “Estimating the location of a tunnel using correlation and inversion of rayleigh wave scattering,” *Geophysical Research Letters*, vol. 40, no. 23, pp. 6084–6088, 2013.

[21] L. A. Konstantaki, D. Draganov, T. Heimovaara, and R. Ghose, “Imaging scatterers in landfills using seismic interferometry,” *Geophysics*, vol. 78, no. 6, EN107–EN116, 2013.

[22] J. Garnier and G. Papanicolaou, “Resolution analysis for imaging with noise,” *Inverse Problems*, vol. 26, no. 7, p. 074 001, 2010.

[23] J. Garnier and G. Papanicolaou, “Correlation-based virtual source imaging in strongly scattering random media,” *Inverse Problems*, vol. 28, no. 7, p. 075 002, Jun. 2012. DOI: 10.1088/0266-5611/28/7/075002. [Online]. Available: <https://doi.org/10.1088/0266-5611/28/7/075002>.

[24] N. M. Shapiro, M. Campillo, L. Stehly, and M. H. Ritzwoller, “High-resolution surface-wave tomography from ambient seismic noise,” *Science*, vol. 307, no. 5715, pp. 1615–1618, 2005.

[25] F.-C. Lin, M. H. Ritzwoller, and R. Snieder, “Eikonal tomography: Surface wave tomography by phase front tracking across a regional broad-band seismic array,” *Geophysical Journal International*, vol. 177, no. 3, pp. 1091–1110, 2009.

[26] M. H. Ritzwoller, F.-C. Lin, and W. Shen, “Ambient noise tomography with a large seismic array,” *Comptes Rendus Geoscience*, vol. 343, no. 8-9, pp. 558–570, 2011.

[27] K. Sager, L. Ermert, C. Boehm, and A. Fichtner, “Towards full waveform ambient noise inversion,” *Geophysical Journal International*, vol. 212, no. 1, pp. 566–590, 2018.

[28] A. Fichtner and V. C. Tsai, “Theoretical foundations of noise interferometry,” in *Seismic Ambient Noise*, N. Nakata, L. Gualtieri, and A. Fichtner, Eds., Cambridge University Press, 2019, ch. 4, pp. 109–143.

[29] B. Müller, T. Hohage, D. Fournier, and L. Gizon, “Quantitative passive imaging by iterative holography: The example of helioseismic holography,” *Inverse Problems*, vol. 40, no. 4, p. 045 016, 2024.

[30] J. Garnier and K. Sølna, “Background velocity estimation with cross correlations of incoherent waves in the parabolic scaling,” *Inverse Problems*, vol. 25, no. 4, p. 045 005, Feb. 2009. DOI: 10.1088/0266-5611/25/4/045005. [Online]. Available: <https://doi.org/10.1088/0266-5611/25/4/045005>.

[31] W. Lambert, J. Robin, L. A. Cobus, M. Fink, and A. Aubry, “Ultrasound matrix imaging—part i: The focused reflection matrix, the f-factor and the role of multiple scattering,” *IEEE Transactions on Medical Imaging*, vol. 41, no. 12, pp. 3907–3920, 2022.

[32] W. Lambert, L. A. Cobus, J. Robin, M. Fink, and A. Aubry, “Ultrasound matrix imaging—part ii: The distortion matrix for aberration correction over multiple isoplanatic patches,” *IEEE Transactions on Medical Imaging*, vol. 41, no. 12, pp. 3921–3938, 2022. DOI: 10.1109/TMI.2022.3199483.

[33] F. Bureau, E. Giraudat, A. L. Ber, *et al.*, “Reflection matrix imaging for wave velocity tomography,” *arXiv preprint arXiv:2409.13901*, 2024.

[34] J. Garnier, L. Giovangigli, Q. Goepfert, and P. Millien, “Probing the speckle to estimate the effective speed of sound, a first step towards quantitative ultrasound imaging,” *Inverse Problems and Imaging*, 2025, ISSN: 1930-8337. DOI: 10.3934/ipi.2026001. [Online]. Available: <https://www.aimscolleges.org/article/id/692581ef1511553245b010e2>.

[35] E. Giraudat, A. Burtin, A. Le Ber, M. Fink, J.-C. Komorowski, and A. Aubry, “Matrix imaging as a tool for high-resolution monitoring of deep volcanic plumbing systems with seismic noise,” *Communications Earth & Environment*, vol. 5, no. 1, p. 509, 2024.